Theory of high-field electron transport and impact ionization in silicon dioxide

D. Arnold,* E. Cartier, and D. J. DiMaria
IBM Research Division, Thomas J. Watson Research Center, Yorktown Heights, New York 10598
(Received 27 December 1993)

A detailed theoretical study of impact-ionization-related transport phenomena in SiO_2 thin films is presented. The Boltzmann transport equation is integrated by the Monte Carlo method using acoustic-phonon-scattering rates derived from photoinduced electron transmission experiments. It is shown that these empirical scattering rates necessitate the inclusion of impact ionization at fields $F > F_{\rm th}^{\rm ii} = 7$ MV/cm because phonon scattering alone can no longer stabilize the electron energy distribution below the ionization energy of 9 eV. However, even above $F_{\rm th}^{\rm ii}$, acoustic-phonon scattering is found to considerably delay the heating of electrons, leading to a wide *dark space* in which impact ionization cannot take place or is strongly reduced. Therefore, the electron multiplication factors $m(F,t_{\rm ox})$ decrease rapidly with decreasing oxide thickness, $t_{\rm ox}$, for $t_{\rm ox} < 30$ nm. These predictions are shown to be consistent with results of several high-field transport experiments in silicon–silicon-dioxide device structures. The calculated electron energy distributions develop high-energy tails which extend beyond the band-gap energy at fields larger than $F_{\rm th}^{\rm ii}$, as observed by vacuum emission experiments. The calculated impact-ionization coefficients are found to be in good agreement with values derived from experiments. The hole generation factors $m-1$ quantitatively agree with substrate hole-current to channel-current ratios measured by the carrier separation technique in *n*-channel field effect transistors with gate oxide thicknesses $t_{\rm ox} \geq 25$ nm. The field and thickness dependence of the measured positive charge buildup (hole trapping) near the Si/SiO_2 interface can be quantified in terms of impact ionization in the oxide film. The calculated carrier multiplication, however, cannot fully account for the substrate hole currents and the hole trapping measured in thinner oxides, $t_{\rm ox} \leq 20$ nm, indicating that another mechanism, likely related to hole injection from the anode, becomes the dominant source for hole currents in thin oxides. Dielectric breakdown of thin SiO_2 films on silicon is reevaluated on the bases of all of these findings. It is proposed that time-dependent breakdown is the result of cumulative degradation of the oxide near its interfaces caused by impact ionization and by hot-electron-induced hydrogen release together. This ansatz is shown to yield a good understanding for the oxide field and thickness dependence of the interface-state generation and of the charge to breakdown. Since impact ionization is strongly suppressed in thin films, $t_{\rm ox} < 25$ nm, degradation and time-dependent breakdown appear to be largely caused by hydrogen release and its subsequent secondary reactions in these thin films.

I. INTRODUCTION

For decades, impact ionization was considered to be the prime cause for dielectric aging and dielectric breakdown in silicon dioxide thin films.[1–10] In much of this early work the model for breakdown was based on the notion of avalanche multiplication fueled by polar-phonon runaway. In this scenario the electron distribution, which is stabilized near thermal energies by longitudinal-optical (LO) phonons at low fields, was believed to become unstable when the electric field increased above some critical value. The electrons would thus rapidly reach energies high enough to initiate impact ionization, starting an electron avalanche by carrier multiplication, and/or causing strong current increases due to field-enhanced current injection because of transient positive space-charge formation and/or hole trapping.[5–7,9,11] In the early eighties, it was first demonstrated by Monte Carlo simulations that the critical field for LO-phonon runaway might be much lower than the measured breakdown fields and electron multiplication might not occur in the proposed manner.[12] This prediction was shortly thereafter confirmed experimentally. The combined results of electroluminescence,[13] carrier separation,[14] and vacuum emission[15] experiments showed that LO-phonon runaway occurs already at 1.5–2 MV/cm, while typical breakdown fields were as high as 10–15 MV/cm. All these results also demonstrated that impact ionization does not occur as proposed earlier, because the electron energy distribution becomes restabilized at *average* energies of only 2–6 eV after LO-phonon runaway. Therefore, a new scattering mechanism different from LO-phonon scattering had to be responsible for the inhibition of impact ionization and breakdown.[16] In the context of laser induced breakdown, it had previously been shown that the inclusion of acoustic-phonon scattering crucially affects the predictions on impact ionization in alkali halides.[17–20] Following Sparks *et al.*[20] Fischetti and co-workers[21,22] incorporated acoustic-phonon scattering in addition to LO-phonon scattering into a Monte Carlo integration of the Boltzmann transport equation for SiO_2 and demonstrated that acoustic scattering can account for the observed energy stabilization at subionization energies. The acoustic rate in the deformation-potential approximation, as proposed by Fischetti, monotonically increases with electron energy,

 ©1994 The American Physical Society

inhibiting impact ionization even at the high breakdown fields of 9–15 MV/cm, typically measured in high-quality oxide films. Shortly after Fischetti's landmark paper, Porod and Ferry published another Monte Carlo model for electron transport in SiO_2.[23] They proposed that intervalley scattering might also contribute to the observed energy stabilization at subimpact-ionization energies. Ferry subsequently investigated impact ionization within this model and concluded that it might occur at lower fields ($F_{th}^{ii}=8$–10 MV/cm).[24] Finally, Bradford and Woolf proposed a third acoustic-phonon-scattering scheme which allowed for impact ionization at even lower fields ($F_{th}^{ii}=3$–4 MV/cm).[25,26] Clearly, no consensus on impact ionization could be reached because the absolute strength and the energy dependence of the electron-phonon interactions differed considerably in these recent models and no experimental data was available to test the validity of the various scattering theories.

Recently, McFeely, Cartier and coworkers[27] proposed a soft-x-ray induced electron transmission technique which yields direct information on the electron-phonon-scattering rates. This zero-field method has the distinct advantage over high-field transport experiments that the scattering rates can be determined as a function of the electron kinetic energy directly. The authors derived an absolute acoustic-phonon-scattering rate in SiO_2 from such experiments[27–29] which differ significantly from all other rates[22,24,25] used for theoretical prediction on impact ionization.

In this paper, we discuss a transport model for SiO_2, which is consistent with the results of these recent zero-field photo-induced electron transmission experiments.[27–29] We propose a semiempirical scattering scheme which accounts for the measured scattering rates and we investigate the consequences of these scattering rates for high-field electron transport and impact ionization using a Monte Carlo integration of the Boltzmann transport equation. We demonstrate that the measured phonon-scattering rates necessitate the inclusion of impact ionization at fields larger than 7 MV/cm, because acoustic-phonon scattering can no longer stabilize the electron energy distribution. Impact ionization itself is found to be responsible for the previously reported[14,15] low average electron energies at fields above 7 MV/cm. We show that acoustic-phonon scattering and impact ionization together stabilize the electron distribution in such a way that no evidence for carrier multiplication by impact ionization can be obtained from the average electron behavior. However, strong support for our transport model is obtained from a series of previously poorly understood high-field measurements in Si/SiO_2 device structures, the results of which can now be directly related to acoustic-phonon runaway and high-field electron multiplication due to band-to-band impact ionization in the SiO_2 gate insulator for $t_{ox} \geq 25$ nm. Acoustic-phonon runaway is shown to yield high-energy tails in the electron energy distributions which extend beyond the impact-ionization threshold as observed by the vacuum emission technique.[30] The calculated hole generation by impact ionization accounts quantitatively for the substrate hole currents in n-channel field effect transistors (FET's) as measured with the carrier separation technique.[31] The magnitude of the positive charge buildup due to hole trapping near the Si/SiO_2 interface[32] can be calculated and some aspects of the interface-state generation by trapped-hole–free-electron recombination[33] can be quantified. The electron multiplication factors obtained by the Monte Carlo method are parametrized by a set of simple analytical expressions which make the Monte Carlo transport results readily available for arbitrary oxide thicknesses and electric-field values, allowing easy calculations of the quantities mentioned above.

If the oxide thickness is smaller than 30 nm, impact ionization is found to be strongly reduced because acoustic-phonon scattering delays the heating of Fowler-Nordheim injected electrons. This induces a wide dark space where impact ionization cannot happen or is strongly reduced as compared to the steady-state condition. The comparison of our calculations with experimental results in this thickness range thus suggest that hole injection from a region close to the anode (possibly related to interface processes[34]) becomes the dominant source of holes.

Previously, we have reported briefly on the capability of the model to explain device properties.[30–32] Here we present a comprehensive discussion of the transport model. The choice of the scattering rates is outlined in Sec. II and the general transport features are discussed in Sec. III. In Sec. IV, we compare the model predictions with experimental results, mostly from Ref. 32, and we discuss the validity and limitations of the model. In Sec. V, we finally reevaluate the role played by impact ionization for dielectric breakdown in Si/SiO_2-based device structures.

II. ELECTRON-TRANSPORT MODEL

Solving the Boltzmann transport equation by the Monte Carlo method[35,36] requires the description of the electron motion in the conduction band structure under the action of the electric field and of the electron scattering in the oxide. The program used is based on Fischetti's original code.[21,22] The electronic states of the conduction electrons are modeled in the extended zone scheme.[20] It has been argued[21,22] that the concepts of a crystalline solid can be applied because SiO_2 has a short-range order similar to that of crystalline forms of SiO_2 and is extending over a distance which is comparable or larger than the scattering length of hot electrons in SiO_2. The conduction band is treated as a single valley with an energy-dependent effective mass. The energy dependence of the electron mass is constructed on the basis of band-structure calculations of α quartz[37] and transport experiments.[38–44] A value of $m_0=0.5m_e$ is used for the mass at the bottom of the band. At high energies, the electron mass is assumed to resume the free-electron value m_e. In the intermediate range, the relative effective mass, m_{eff} is assumed to increases linearly starting at 2.25 eV such that it reaches m_e at 4.5 eV. This interpolation is preferred over the slightly different interpolation used in Ref. 22 because it allows a more accurate calculation of the energy-dependent electron mean free path as measured with internal photoemission.[44] Such an energy

dependence of the mass leads to a rapid increase in the density of states above 2.25 eV, as observed by inverse photoemission experiments.[45] A polaron corrected mass has previously been considered.[21] Recently, Jensen and Sauls[46] demonstrated that the electrons rapidly decouple from the LO phonons as their energies increase. A polaron corrected mass is therefore important at small electron energies only and is neglected in this study. This is justified because impact ionization is controlled by acoustic-phonon scattering at much higher energies, as will be shown.

Scattering mechanisms included in the Monte Carlo analysis are LO-phonon scattering with the 63- and 153-meV modes, acoustic-phonon scattering including the phonon dispersion, and impact ionization. Scattering with the LO phonons is treated with the usual Fröhlich Hamiltonian[21] using optical constants as measured by Lynch.[4] Measurements with high-resolution electron-energy-loss spectroscopy indicate that this approach is valid over the whole energy range of interest here.[47] Electron scattering with acoustic phonons is based on the rates derived from photon-induced electron transmission experiments.[29,44,48] At low energies, these measured rates are well represented by the deformation-potential theory using a deformation potential of 6 eV and the band structure discussed above, confirming the validity of the approach used by Fischetti *et al.*[22] The acoustic-phonon-scattering rate, $1/\tau_{ac}(w)$, can thus be calculated from the equation,[49]

$$1/\tau_{ac}(w)=\frac{3m_{eff}C_{ac}^2}{4\pi\rho\hbar k}\int_{q_c}^{q_{max}}\frac{q^3}{\hbar\omega(q)}\left(\tfrac{1}{2}\pm\tfrac{1}{2}+n_q\right)dq \;. \tag{1a}$$

k and q are the electron and the phonon wave vector, respectively, $q_c=2m_0c_s$, $c_s=4.6\times10^5$ cm/sec is the polarization-averaged velocity of sound, $q_{max}=2k-q_c$, C_{ac} is the electron-acoustic phonon-coupling constant, ρ the SiO_2 density, and n_q the Bose function at wave vector q and temperature T. The phonon dispersion is approximated as[49]

$$\hbar\omega(q)=(2/\pi)\hbar k_{BZ}c_s[1-\cos(\pi q/2k_{BZ})]^{1/2} \quad \text{for } (q<k_{BZ}) \tag{1b}$$

$$\hbar\omega(q)=(2/\pi)\hbar k_{BZ}c_s \quad \text{for } (q\geq k_{BZ})\;, \tag{1c}$$

where $k_{BZ}=1.208\times10^8$ cm^{-1} is the wave vector at the edge of the first Brillouin zone (BZ). The integration over the q vector is performed numerically. Equation (1a) is not expected to be correct at high energies since the acoustic rate diverges and does not approach the elastic-scattering rate as derived from phase-shift calculations.[26] Two independent studies[26,50] showed that the acoustic rate might actually decrease with $E^{-1/2}$ at high energies, rather than increase with $E^{3/2}$ as in Eq. (1a). In one theory,[26] a Coulombic-type screening[51] was introduced in the deformation-potential matrix element, while the second study used a different integration over the final states in the Umklapp-dominated scattering regime at high energies.[50] The predicted $E^{-1/2}$ dependence at high energies appears to be consistent with the experimental data of Cartier and McFeely.[29] An accurate parametrization of these experimental results over the whole energy range from thermal energies to 16 eV, however, is difficult within these models. If we use the approach of Bradford and Woolf, for example, it is not possible to find a set of parameters (deformation potential and screening length) which account for the results of the electron transmission experiments at low[44] and high[29] energies simultaneously. This happens because the screening, even so less effective at low energies, remains too strong. Possibly, this difficulty could be overcome if the density of states were included in the calculations in a more rigorous way. Inverse photoemission experiments by Himpsel and Straub[45] indicate that the empty density of states might actually decrease above 6 eV. Such a decrease is expected to reduce the electron-phonon scattering rates at high energies[52,53] and would thus allow the use of weaker screening. A more fundamental calculation of the acoustic-phonon-scattering rates might be difficult for yet another reason. The phonon-scattering rates derived from the electron transmission experiments have absolute values of the order of 5×10^{15} sec^{-1}, implying very short times between scattering events. It might be questioned whether a classical Monte Carlo transport formalism (using first-order-scattering rates) can provide a physically correct description of the electron motion when the electron-phonon scattering is so strong. Attempts have been made to include quantum effects by solving the Dyson equation instead of using the Fermi Golden rule.[54] However, besides numerical problems, there are still considerable unsolved conceptual difficulties with this method[54] and it is beyond the scope of this paper to explore further the possibilities of this approach. Because of all these uncertainties, we have used a semiempirical approach and accurately parametrized the experimental scattering rates by modifying Eq. (1a) at high electron energies. We found that this can be achieved by assuming that the wavelength of acoustic phonons has to be larger than some critical value, λ_{min} which we expect to be of the order of twice the interatomic distance in the solid. The existence of such a minimum wavelength limits the upper integration boundary in Eq. (1a) to a maximum value of

$$q_{max}\leq 2\pi/\lambda_{min} \tag{1d}$$

and the scattering rate decreases with $E^{-1/2}$ for electron wave vectors $k\geq(2\pi/\lambda_{min}-q_c)/2$. An excellent parametrization of the experimental rates[29] is obtained with a value of $q_{max}=0.235$ nm^{-1}, maintaining a deformation potential of $C_{ac}=6$ eV at all electron energies. With these two values, Eqs. (1a) to (1d) yield a maximum in the acoustic rate at an electron energy between 5 and 6 eV. We demonstrate below that the classical Monte Carlo method together with this semiempirical acoustic scattering rate allows accurate predictions on high-field hot-electron effects in SiO_2. Our semiempirical methodology thus provides a powerful tool for high-field transport studies in wide band-gap insulators, where first-principles calculations cannot be performed easily: The scattering rates were determined from *zero-field* transport experi-

ments by means of the same Monte Carlo transport formalism,[29] such that subsequent high-field simulations, using Eqs. (1), differ only with respect to the electric-field term in the transport equation.

The impact-ionization rates are derived from experimental studies as well. Here, the Keldysh formula,

$$\frac{1}{\tau_{\rm ii}}=P_{\rm ii}\left[\frac{E}{E_{\rm th}}-1\right]^2 , \qquad (2)$$

is used to parametrize available experimental data. We used the rates from two sources. Namely, deep inelastic rates as derived from electron transmission experiments[29] and impact-ionization rates as derived from the measured dielectric function.[25] The difference between these results is likely caused by the high sensitivity of electron transmission experiments to interface processes, which can contribute to the deep inelastic rate.[29] We therefore favored the optical measurements at low energies, choosing a value of $P_{\rm ii}=1.3\times10^{15}$ $\rm sec^{-1}$ for the prefactor, and of $E_{\rm th}=9$ eV for the impact-ionization threshold. The large spread in the existing experimental data leaves considerable errors in these two parameters. However, it will be shown later (by varying these parameters) that impact ionization is largely controlled by the phonon processes below the ionization threshold and not by the ionization rate itself. Reasonably accurate predictions of high-field impact ionization are therefore possible despite the rather poor knowledge of the ionization rate as a function of energy.

The resulting scattering rates at 300 K are summarized in Fig. 1. The different energy dependences of the various interactions lead to two distinctly different transport regimes on the electron-energy scale, which can also be observed by varying the electric field, as will be shown in the next section. The two regimes on the energy scale can be more clearly seen from Fig. 2, which shows the momentum [panel (a)] and the energy [panel (b)] relaxation rates, corresponding to the scattering rates of Fig. 1. For the purpose of illustration, these quantities were simply calculated as the rate of energy (momentum) change divided by the energy (momentum), considering scattering out of the electron states only. From Fig. 2(b), it can be seen that the large energy of the LO phonons leads to strong energy relaxation near 153 meV (the energy of the dominant LO mode). The LO rate rapidly decreases towards higher energies because of the Coulombic nature of the interaction. In contrast, acoustic phonons which have small energies, contribute little to the energy relaxation rates even at energies where the acoustic rate is much higher than the LO rate. Only above the ionization threshold does the energy relaxation rate rise strongly again because of the deep inelastic nature of impact ionization. The momentum relaxation rates shown in Fig. 2(a) have very different energy dependences. LO-phonon scattering favors small angle scattering providing little momentum relaxation. In contrast, acoustic-phonon scattering favors large angle scattering and the momentum relaxation rate has absolute values which are close to those of the acoustic scattering rate itself. The existence of a maximum in the momentum relaxation rate below the ionization threshold is of particular importance for a quantitative understanding of impact ionization.

In order to study the high-field electron dynamics in thin oxide films, we solved the Boltzmann equation in the

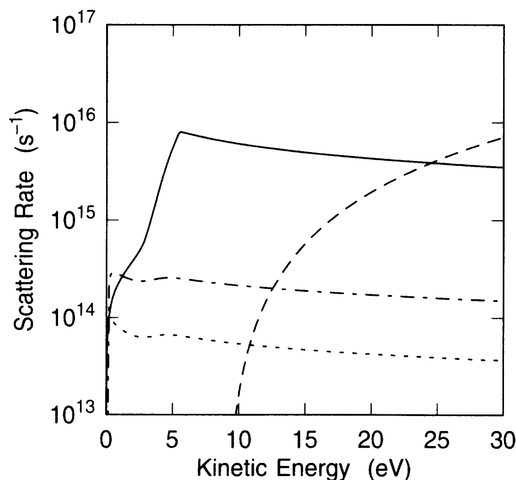

FIG. 1. Semiempirical scattering rates in SiO_2 at 300 K as a function of the electron kinetic energy. The solid curve is the acoustic-phonon scattering rate [Eq. (1)], the dashed curve is the impact-ionization rate [Eq. (2)], the dot-dashed curve is the 153-meV LO-phonon-scattering rate, and the dotted curve is the 63-meV LO-phonon scattering rate.

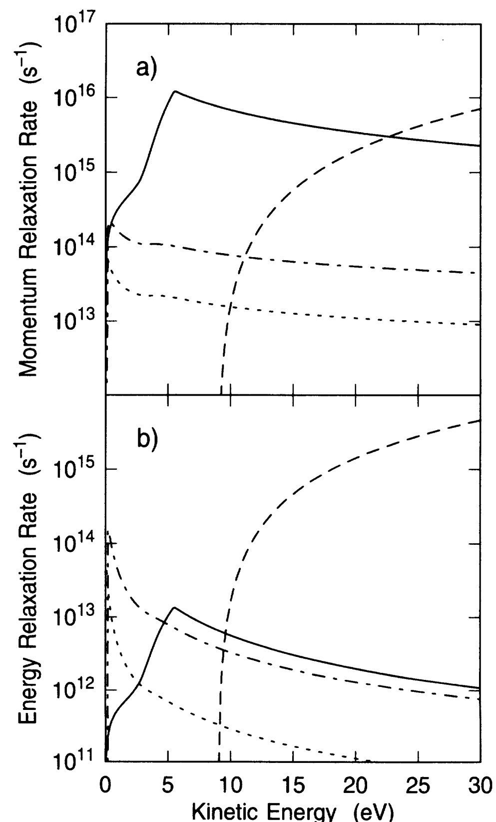

FIG. 2. Momentum relaxation rates [panel (a)] and energy relaxation rates [panel (b)] in SiO_2 versus electron kinetic energy. For identification of the various curves see caption of Fig. 1.

thickness range, $10 < t_{ox} < 100$ nm, for homogeneous electrical fields, $F < 20$ MV/cm. In a few cases, we have also investigated nonhomogeneous field situations to study the influence of space-charge formation in the oxide. In all cases, the electrons were injected at zero energy into the high-field region of the films (Fowler-Nordheim tunneling through a 3.1-eV-triangular barrier). We calculated electron densities, $n(E_j)$, by tabulating the electron energies, E, during the total electron transit time at a given film thickness, t_{ox}, and a given electric-field configuration. Typically, sample sizes of 10^3-10^4 electrons were employed to acquire sufficient statistics. The average electron energies are calculated from the normalized electron densities as,

$$E_{av} = \sum_{j=1}^{k} n(E_j) \times E_j \ , \tag{3}$$

where k is the number of energy bins used. The electron multiplication factors are given by,

$$m = 2^{\alpha t_{ox}} \ , \tag{4}$$

where

$$\alpha(F, t_{ox}) = v^{-1} \sum_{j=1}^{k} \frac{n(E_j)}{\tau_{ii}(E_j)} \ . \tag{5}$$

The average velocity, $v = t_{ox}/\tau_{trans}$ (τ_{trans} is the average transit time in the film), approaches the drift velocity in the thick-film limit. The quantity α, as defined in Eq. (5), depends on the oxide field *and* on the oxide thickness. In the limit of thick oxides, α resumes the usual t_{ox}-independent definition for the impact-ionization coefficient. The average number of impact-ionization events per injected electron is equal to $m-1$. This quantity is also equal to the average number of holes generated per injected electron and is referred to as the "hole generation factor."

III. ELECTRON-TRANSPORT RESULTS

A. Average electron energy

At fields below 7 MV/cm we calculate essentially the same average electron dynamics as that published previously by Fischetti.[21] This is not surprising, since our rates only differ significantly from those used by Fischetti at electron energies above 6 eV. Up to fields of 7 MV/cm, electrons do not frequently enter this energy range. Above 7 MV/cm however, we obtain dramatically different results. The features of our model can be seen most easily from the calculated average electron energies as summarized in Fig. 3. We compare results of three different simulations. In the first simulation (dotted line), we considered scattering with LO phonons only. As can be seen, the electrons are stabilized by the LO phonons up to a field of 1.5 MV/cm only. At higher fields, the electrons gain more energy from the field than they can lose to the LO phonons and the entire electron population runs away from the maximum in the energy-loss rate around 150 meV.[12] The second simulation (dashed line), also includes acoustic-phonon scattering (see Fig. 1).

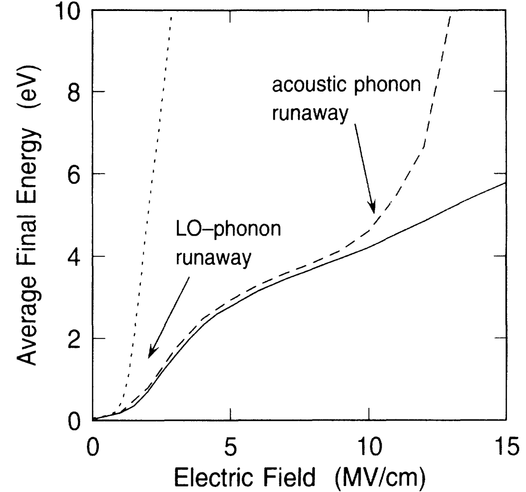

FIG. 3. Comparison of calculated average electron energies versus electric field for three scattering models: 1. Scattering with longitudinal-optical phonon only (dotted curve), 2. Scattering with LO and acoustic phonons (dashed curve), 3. Impact ionization in addition to scattering with all phonon modes (solid curve). The energies correspond to the average final energy after transport through a 50-nm-oxide film. The scattering rates used are those from Fig. 1. The figure serves to illustrate how the electrons get restabilized by acoustic phonons after LO-phonon runaway and by impact ionization after acoustic-phonon runaway.

Acoustic scattering prevents impact ionization after LO-phonon runaway by restabilizing the electron distribution at average energies of 2–4 eV.[21] The average electron energy increases very gradually, even though the electrons lose energy to the lattice slowly [see Fig. 2(b)]. This is possible because they cannot gain energy rapidly from the electric field, since they are strongly scattered in random directions by acoustic phonons [see Fig. 2(a)]. The difference between the two transport regimes below and above the LO-phonon runaway threshold was beautifully illustrated by Fischetti, who calculated the actual electron trajectories.[21] Below 2 MV/cm, transport occurs in a streaming-type fashion (forward LO-phonon scattering) while the motion is dispersive at higher fields (large-angle acoustic scattering). We find now that *the maximum in the acoustic rate at about 6 eV [see Fig. 2(a)] leads to an electron runaway phenomenon similar to LO-phonon runaway*. The electrons start to escape from the acoustic phonons at 7 MV/cm and the whole distribution becomes unstable at about 10 MV/cm for the 50-nm film shown in Fig. 3, leading to average electron energies larger than the impact-ionization threshold. The carrier runaway is more sluggish in this case because of the dispersive nature of the transport and the large width in energy of the maximum in the acoustic rate. In the final simulation (solid line in Fig. 3), impact ionization is included as well. The large energy relaxation during impact ionization restabilizes the energy distribution and leads to average energies which are almost identical to those previously derived by Fischetti even though he considered the electrons to be stabilized by acoustic phonons alone. This similarity in the average energies arises from the fact that

the electrons become part of the main portion of the energy distribution after impact ionization. Evidently, *in sharp contrast to LO-phonon runaway, acoustic phonon runaway and impact ionization cannot be predicted from the measured average electron behavior.* However, the comparison of our model predictions with results from vacuum emission and carrier separation experiments presented in Sec. IV strongly support the importance of acoustic-phonon runaway and impact ionization at fields above 7 MV/cm.

B. Electron-energy density

1. Field dependence

Typical electron-energy densities $n(E)$ obtained by space-time averaging of the electron energies during transport through a 50-nm-oxide film under homogeneous fields of 5, 7, 9, and 11 MV/cm are shown in Fig. 4. For fields larger than 7 MV/cm, high-energy tails extending beyond the gap energy are found to develop rapidly with increasing field strength. However, the average electron-energy increases only gradually with field, essentially tracking the energy of the peak in the energy density, as can be seen by comparing Figs. 3 and 4. The underlying transport physics can be understood by looking at the instantaneous kinetic energy of a typical sample electron. As shown in Fig. 5, such an electron spends most of its time at energies where the momentum relaxation is a strongly increasing function of energy. Once it climbs above the maximum in the acoustic rate it generally accelerates quickly until it loses most of its kinetic energy in an impact-ionization event and become part of the main portion of the distribution. *At fields above 7 MV/cm, our model thus predicts a continuous flow of electrons to energies larger than the impact-ionization threshold (high-energy tail), while the average energy remains of the order of 5 eV only.* In the absence of impact ionization, the distribution would be unstable, as shown in Fig. 3. The high ionization energies in Fig. 5 (12 and 18 eV) reflect the nature of the soft ionization threshold in Eq. (2) and cause the energy tails in Fig. 4 to extend well above the energy of the band gap.

2. Thickness dependence

The broad maximum in the acoustic scattering rate leads to a delayed formation of the high-energy tails, as illustrated in Fig. 6. The figure shows the evolution of $n(E)$ during the heat-up process in a 50-nm-thick oxide after Fowler-Nordheim injection at a field value of 10 MV/cm. These distributions were calculated by space-time averaging over five 10-nm-thick regions within the oxide layer as described by the legend in the figure. The slow, transient formation of the high-energy tail over a thickness range of 30 nm is in sharp contrast to the much shorter distance of about 3–5 nm (Ref. 22) required to essentially establish the steady-state average electron energy. Again, this happens because the electrons can gain energy only slowly once they enter the dispersive transport regime above 3 eV. As a consequence, *there exists a broad spatial region in which the electron energies do not exceed the ionization threshold even at fields above 7 MV/cm, leaving a wide dead space (dark space)*[55,56] *where impact ionization is not possible or strongly reduced.*

C. Impact ionization

The effect of the dark space on impact ionization in thin films is quite dramatic. This can be seen from Fig. 7, which shows calculated electron multiplication factors, m (plotted as $m-1$), as a function of the electric field for oxide thicknesses in the range $10 < t_{ox} < 100$ nm. The symbols are values calculated from energy densities as shown in Fig. 4 using Eqs. (4) and (5). The solid and dashed curves correspond to an analytical parametriza-

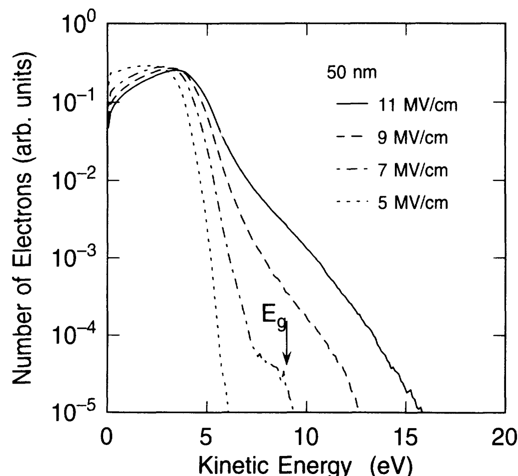

FIG. 4. Space-time-averaged electron densities in a 50-nm-thick oxide at fields from 5 to 11 MV/cm, calculated by using all scattering processes shown in Fig. 1. A high-energy tail extending beyond the band-gap energy of $E_g = 9$ eV is found to form for electric fields larger than 7 MV/cm.

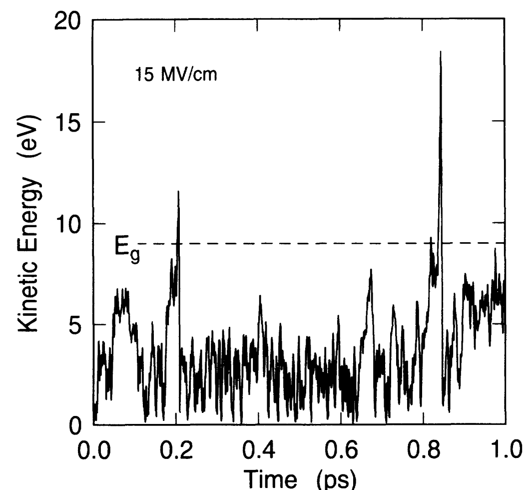

FIG. 5. Calculated instantaneous kinetic energy of a typical sample electron at an electric field of 15 MV/cm using the rates of Fig. 1. Impact ionization occurs at times of 0.2 and 0.85 psec. The high ionization energies of 12 and 18 eV reflect the soft threshold used for the impact-ionization rate in Eq. (2).

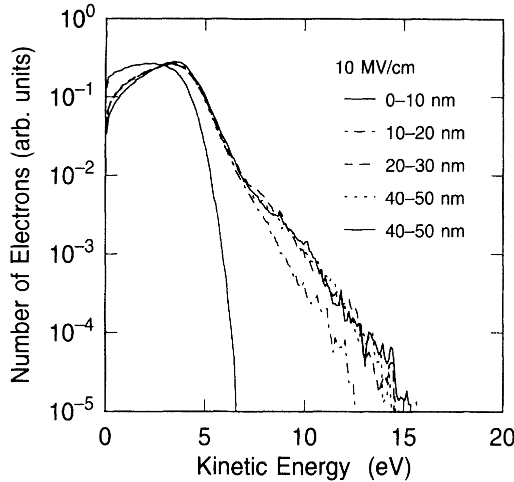

FIG. 6. Calculated evolution of the electron density after Fowler-Nordheim injection. The electric field is 10 MV/cm. The scattering rates used are those shown in Fig. 1. Each density was calculated by space-time averaging over consecutive 10-nm-thick slabs as indicated by the inset. The average electron energy is in quasi-steady-state after 10 nm but the high-energy tail does not fully form until electrons penetrate 20–30 nm into the oxide.

tion of the Monte Carlo results according to Eqs. (6)–(8).

$$m-1=P_{\mathrm{mf}}\left[\frac{F}{F_{\mathrm{th}}^{\mathrm{ii}}}-1\right]^4 , \tag{6}$$

where all fields are in MV/cm and the values for the threshold field and the prefactor are given by

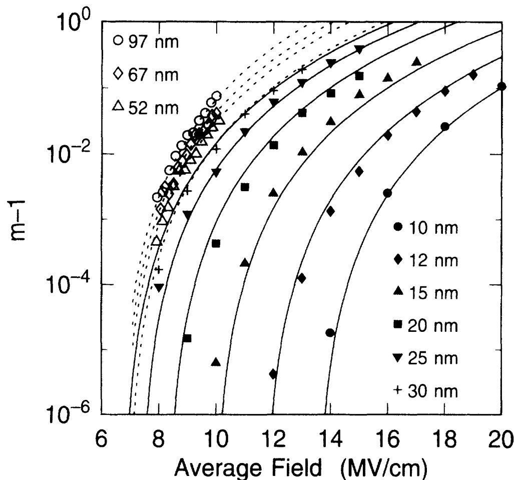

FIG. 7. Calculated electron multiplication factors m for oxide thicknesses from 10 to 97 nm. The symbols are results obtained directly from the Monte Carlo simulation via Eqs. (4) and (5) using the rates shown in Fig. 1. The solid and dashed lines represent an analytical parametrization of the Monte Carlo results as given by Eqs. (6)–(8). The strong thickness dependence for $t_{\mathrm{ox}}<30$ nm is due to the transient formation of the high-energy tail in the electron distribution (dark space), as shown in Fig. 6.

$$F_{\mathrm{th}}^{\mathrm{ii}}=F_{\mathrm{th}}^{\infty}\left[1+\frac{t_1}{t_{\mathrm{ox}}-t_d}\right] \tag{7}$$

and

$$P_{\mathrm{mf}}=P_0(t_{\mathrm{ox}}-t_d)+P_1\frac{1}{t_{\mathrm{ox}}-t_d} . \tag{8}$$

The values $F_{\mathrm{th}}^{\infty}=6.4$ MV/cm, $t_d=8.2$ nm, $t_1=1.56$ nm, $P_0=9\times10^{-3}$ nm^{-1}, and $P_1=3.0$ nm, should be used for $t_{\mathrm{ox}}>30$ nm (dashed curves in Fig. 7), while a more accurate parametrization below 30 nm is obtained by using $F_{\mathrm{th}}^{\infty}=3.8$ MV/cm, $t_d=1.5$ nm, $t_1=21.6$ nm in Eq. (7) and $P_0=0$, $P_1=5.5$ nm, $t_d=7$ nm, in Eq. (8) (solid curves in Fig. 7). These parametrizations allow a reasonably accurate calculation of electron multiplication factors at arbitrary film thicknesses and oxide fields without further use of the time-consuming Monte Carlo algorithm and they are used below for comparison with experimental data. The functional forms of Eqs. (6) to (8) reflect the transport physics discussed previously. The singularity at $t_{\mathrm{ox}}=t_d$ in Eq. (7) accounts for the formation of the dark space in thin films and leads to a rapid shift of the ionization threshold to higher-field values with decreasing thickness. At large thicknesses, the threshold field reaches the constant value, F_{th}^{∞}, corresponding to steady-state transport. The linear term in Eq. (8) reflects the linear dependence of the multiplication factor on thickness under steady-state conditions, while the strong increase at small thicknesses (hyperbolic term) can be understood as the transition into the ballistic transport regime where the multiplication factor is expected to track the strong energy dependence of the ionization rate more directly.

The calculation of electron multiplication factors can be used to gain further insight into the role played by various scattering processes in high-field transport. This is illustrated by performing three additional simulations using scattering rates which deviate from the nominal values in Fig. 1 as shown in Fig. 8. The solid curves show the acoustic phonon and impact ionization rates used previously. The broken curves show rates resulting from the following single parametrization changes in Eq. (1a) and Eq. (2): The dashed line is obtained with $E_{\mathrm{th}}=8$ eV, the dotted line with $P_{\mathrm{ii}}=1.8\times10^{15}$ sec^{-1}, and the dashed-dotted line with $k_{\max}=0.23$ nm^{-1}. The corresponding changes in the calculated multiplication factors are summarized in Fig. 9, using the 51.7-nm film as an example. Clearly, significant changes in the ionization rates have little effect on m. A much smaller change in the acoustic scattering rate, however, changes m considerably. The instantaneous kinetic energy shown in Fig. 5 provides a simple explanation for these somewhat unexpected dependences. In short, the magnitude of the multiplication factor is essentially determined by the average time between two ionization events. As can be seen, the sample electron in Fig. 5 spends most of the time in the dispersive transport regime near 6 eV. Once an electron reaches energies close to E_{gap}, it tends to accelerate quickly to energies where the impact-ionization rate is large. As a consequence, *m is largely independent of the*

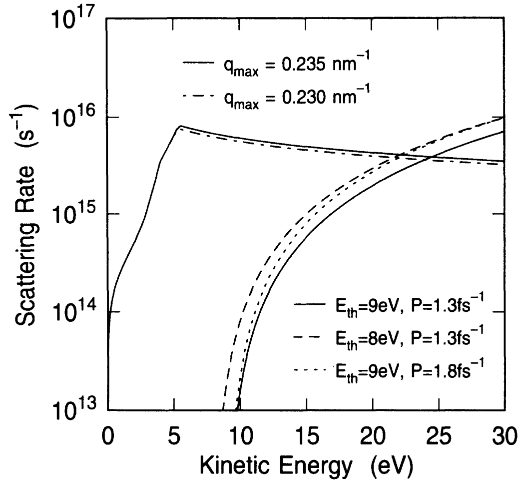

FIG. 8. Acoustic-phonon-scattering rates and impact-ionization rates used to test the sensitivity of the calculated electron multiplication factors to the absolute magnitude of the scattering rates used in the transport model. Acoustic scattering rates are shown for two values of the maximum phonon wave number q_{max} in Eq. (1a). Impact-ionization rates are shown for three combinations of the threshold energy, E_{th}, and the prefactor, P, in the Keldysh formula [Eq. (2)]. The solid curves show the nominal rates of Fig. 1.

impact ionization rate but it depends critically on the magnitude of the acoustic rate below the ionization threshold. A similar conclusion has recently been reached for impact ionization in silicon.[57] The fact that the acoustic rate is a decreasing function with energy amplifies this effect in SiO_2 and the still poorly known threshold energy for impact ionization has relatively little influence on the calculation of multiplication factors in thick films at high fields. However, in thinner oxides where transport is quasiballistic, multiplication factors will depend more strongly on the absolute value of the ionization threshold.

These additional calculations also yield a rough estimate for the accuracy of the calculations. The error in the cutoff wave vector in Eq. (1d)—as determined from the soft-x-ray experiments—is of the same order as the variation used in Fig. 8. Similarly, the uncertainties in the ionization threshold and the prefactor in Eq. (2) are comparable to the variations used in Fig. 8. Therefore, the differences between the various curves in Fig. 9 yield a measure for the absolute accuracy of the calculated multiplication factors.

IV. COMPARISON WITH EXPERIMENT

A. Vacuum emission

Vacuum emission from MOS(metal-oxide-silicon)-capacitor structures has been widely used to investigate the high-field electron dynamics in SiO_2.[10,15,49,58–62] The method determines the energy distribution of electrons emitted from the anode into vacuum after transport through an oxide film under the action of an electric field. The electrons are injected by Fowler-Nordheim tunneling. The dotted curve in Fig. 10 shows the simulated energy distribution of electrons crossing a virtual boundary after transport through 50 nm of oxide at 10 MV/cm. This distribution represents the result of an idealized vacuum emission experiment in which the scattering in the top contact (metal gate) can be neglected. As can be seen from Fig. 10, a vacuum emission experiment does not measure the space-time-averaged electron density (solid curve). Vacuum emission experiments preferentially sample high-energy electrons. In vacuum emission, each electron exiting the film is counted with the same statistical weight, while space-time averaging gives more weight to electrons with low velocities (long transit times). Also,

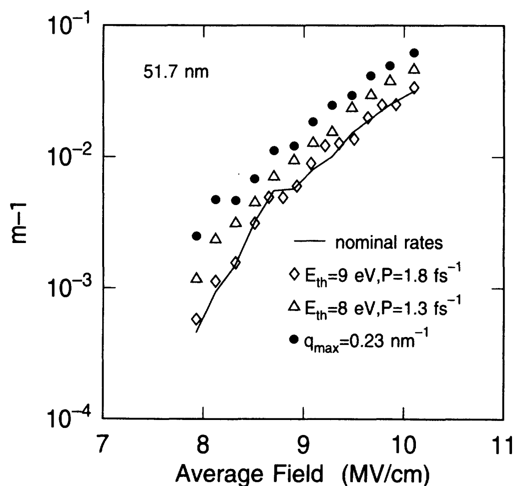

FIG. 9. Calculated electron multiplication factors, m, using the scattering rates shown in Fig. 8. The calculations illustrate that variations in the magnitude of the impact-ionization rate have little effect on the model predictions (compare solid line with open symbols). Impact ionization is largely controlled by the magnitude of the acoustic scattering rate at high energies (compare solid line with full dots).

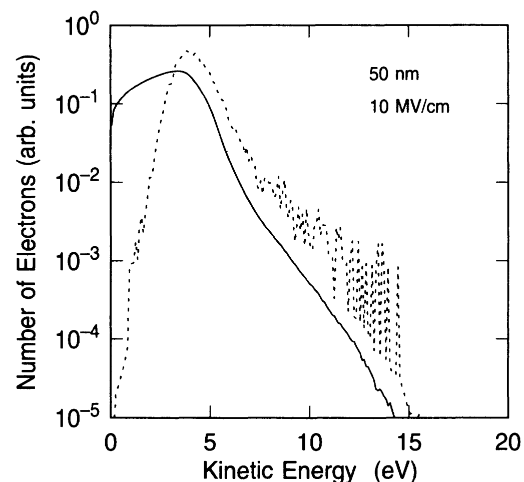

FIG. 10. Comparison of the space-time-average electron density in a 50-nm-thick oxide (solid line) with the surface electron density which represents a snapshot of the exiting electron population after transport through a 50-nm oxide (dashed line). Effects due to the oxide-vacuum interface and the metal gate electrode have been neglected.

electrons emitted into vacuum are always accelerated on their final path before emission, while the energy density also includes carriers which get decelerated by the field because they move towards the injecting contact.

All vacuum emission experiments in SiO_2 (Refs. 10, 15, 49, and 58–62) have been done by using retarding-field electron-energy analyzers. These instruments yield the energy distribution function, $N(E)$, which is the integral of the electron-energy density,

$$N(E)=\int_E^{\infty} n(E')dE' , \tag{9}$$

where $n(E)$ is the proper energy density for vacuum emission as discussed above. Typical distribution functions measured with a 51.7-nm-oxide film and a 17-nm-thick aluminum electrode are shown in Fig. 11 [panel (a)] for anode fields of 6.6–9.7 MV/cm.[31] Figure 11 [panel (b)] shows the calculated, idealized distribution functions (neglecting carrier relaxation in the metal gate) emitted from a 50-nm-thick film at constant oxide fields of 7–10 MV/cm. As can be seen by comparing Figs. 11(a) and 11(b), the measured evolution of the high-energy tails with field is well accounted for by the calculations, confirming the need of a soft threshold for impact ionization. At energies below 5 eV, the simulations appear to be less accurate. This is due to the neglect of transport through the thin top gate electrode. Recent simulations by Bradford and Woolf[25] confirm earlier speculations[15] that the measured high-energy tails are due to electrons which are emitted in an "ideal manner" (without extra attenuation) through cracks or voids in the gate metal, while the low-energy portion of the distribution also includes contributions of higher-energy electrons which have lost additional energy by Coulombic scattering in the gate. This extra scattering has been shown to qualitatively account for the differences between Figs. 11(a) and 11(b) at low energies.[25] In thicker oxides, electrons with energies of the order of 20 to 40 eV have been reported.[15,62] Such high energies are inconsistent with our calculations. It can be shown easily that the electrostatic fields around emitting voids or cracks in the metal gate do extend into vacuum and allow for considerable energy gain after emission. These energy gains are larger in thick oxides because the applied voltages are higher.

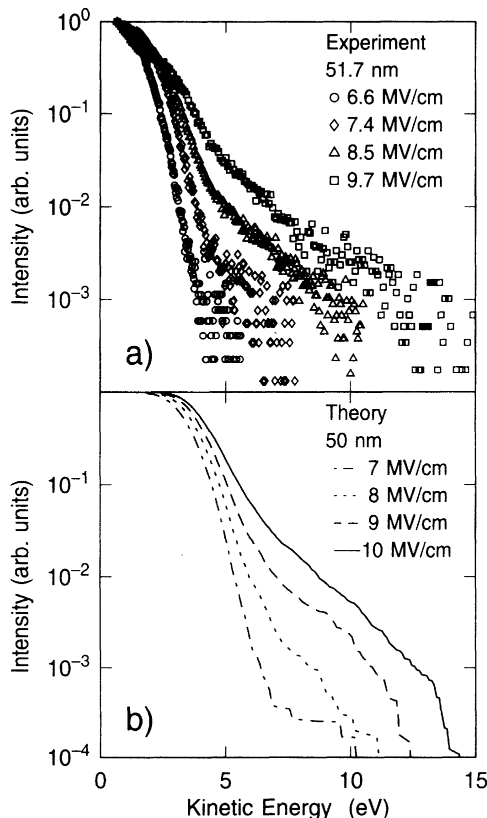

FIG. 11. Comparison of measured [panel (a)] and calculated [panel (b)] electron distribution functions for an oxide thickness of about 50 nm and fields from 7 to 10 MV/cm. The observed high-energy tails extending above the band-gap energy of 9 eV are predicted by the transport model.

The experimental field values given in Fig. 11(a) correspond to the anode fields, which are larger than the average fields because of net negative space-charge formation during the experiments.[15] Our calculations in inhomogeneous fields confirm that the anode field is the controlling field. Distributions calculated in the presence of space charge as encountered in the experimental situation were found to be equal to the distributions calculated without space charge but at a constant field equal to the anode field. The field distortions during the experiment are not large enough to prevent a quasi-steady-state adjustment of the electron distributions to the field variation.

B. Substrate hole currents in *n*-channel field-effect transistors (FET's)

Measured substrate hole currents in *n*-channel FET's, using the carrier separation technique,[14,30,63–68] provide another test for our calculations. The method is schematically depicted in Fig. 12. The source and drain contacts of the FET are grounded. Electrons from the channel tunnel into the high-field region in the oxide and

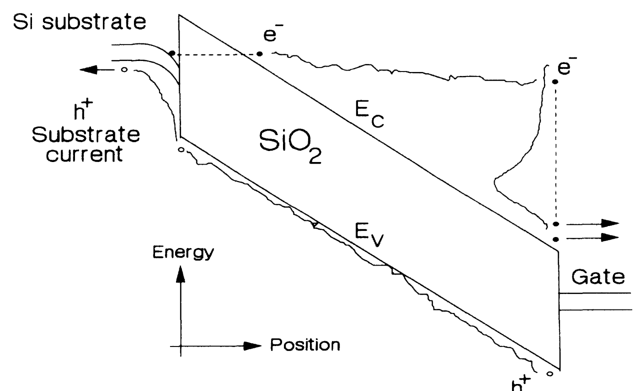

FIG. 12. Schematic energy diagram of an *n*-channel field effect transistor illustrating the principle of the carrier separation experiment used to measure hole currents created by band-to-band impact ionization in the gate oxide.

travel to the gate. If the electrons gain energy in excess of the ionization threshold, electron-hole pairs will be generated in the oxide. The holes travel back to the cathode and are collected as a substrate hole current. If all holes are collected with an efficiency of one by the substrate and if impact ionization is the only source for holes, then the measured ratio of the substrate hole current, I_s, to the channel current, I_c, is directly related to the electron multiplication factor as defined in Eq. (4),

$$\alpha_{\exp} \equiv \frac{I_s}{I_c} = m - 1 \ . \tag{10}$$

Many of the conditions, for Eq. (10) to be valid, are known to be satisfied. Hole transport in SiO_2 is known to be so dispersive that the holes remain close to the valence-band maximum even at fields of the order of 10 MV/cm.[69,70] Therefore, hot-hole multiplication in the oxide does not occur. Similarly, we do not expect significant hole multiplication in the Si substrate because the hot holes rapidly thermalize in Si due to strong phonon coupling.[53] The collection efficiency of the holes is essentially unity because the holes are rapidly swept out of the depletion region preventing electron-hole recombination. This has been directly tested by substrate bias experiments. Finally, the fraction of holes trapped in the oxide is small as shown in the next section.

In Fig. 13, we compare calculated hole generation factors, $m - 1$, due to impact ionization in the oxide using Eqs. (6)–(8) and (10) with as-measured current ratios,

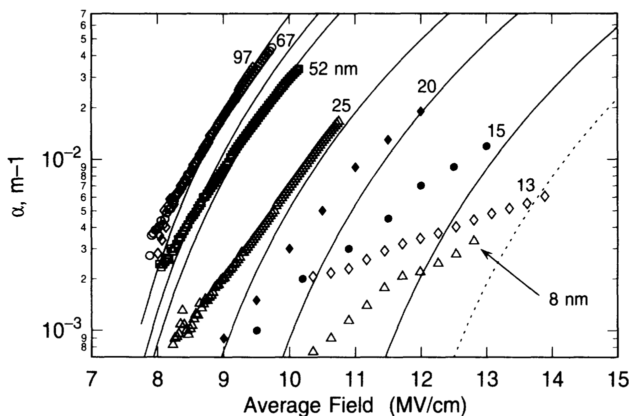

FIG. 13. Comparison of as-measured (α, symbols) and calculated ($m - 1$, lines) hole generation factors, as a function of oxide field for oxide thicknesses from 8 to 97 nm. The thickness values are placed at the high end of the corresponding experimental data and closest to the corresponding calculated curve. The measured values were derived from carrier separation experiments in n-channel field effect transistors using Eq. (10). The open symbols show data measured by us (Ref. 32), while the full symbols show data extracted from measurements by Chen, Holland, and Hu (Ref. 68). As can be seen, the calculated curves and the experimental data converge at high fields for each thickness. This is the range where most of the holes are generated by impact ionization. In thin oxides and at low fields, an "excess" hole current is measured which can be attributed in part to anode-hole injection and to hole currents caused by generation recombination in the silicon (for details, see text).

$\alpha_{\exp}$, as defined by Eq. (10). Data shown by open symbols are from Ref. 32, while data shown by solid symbols are calculated from current measurements of Chen, Holland, and Hu.[68] For any given oxide thickness, the measured current ratios converge towards the theoretically predicted values at high fields (or large current ratios), only. Near the low-field end of each data set, where the contribution by impact ionization is predicted to be small or zero, the agreement is poor. The discrepancy becomes more severe with decreasing oxide thickness.

To verify whether some of the deviations in Fig. 13 arise from charge trapping during the experiments (see Sec. IV D), we included oxide space charge into the calculations in a few cases. At low fluencies, holes are trapped near the cathode interface, leading to a smaller field in the bulk of thick films and to a corresponding decrease in the multiplication factor. We find, that this effect could account for some of the irregularities seen in the thick films. In thinner films, trapped hole densities are too small to have an effect. With increasing fluency, trapped holes become rapidly compensated by electron trapping leading to net negative space charge. We find that *homogeneous* negative space charge has little effect on the space-time-averaged energy densities and on the multiplication factors. This happens because the effect of the field reduction near the cathode is largely compensated by the field enhancement near the anode.

Provided that our calculations are accurate, the discrepancies between theory and experiment in Fig. 13 have to be attributed to processes other than impact ionization in SiO_2. Several such processes have previously been discussed. Generation-recombination (GR) centers in the silicon are known to be an efficient source of substrate hole currents because thermal generation of electron-hole pairs in the substrate is trap assisted. An accurate correction for GR currents is difficult because new generation-recombination centers can be created during the measurement itself, as discussed in Ref. 32. From this and other studies, it is clear, however, that GR currents cannot fully account for the discrepancies between experiment and theory reported in Fig. 13, especially for oxide thicknesses in the range from 6 to 20 nm. Hole injection at or near the anode by electronic processes is believed to occur. A variety of microscopic anode hole-injection mechanisms have been proposed:[34,66,67] Hot-electron-induced hole injection from the anode into the oxide (via interface plasmon excitation[34]); Hot-electron-induced electron injection from the oxide valence band directly into the conduction band of the anode material; Ionization of states in the gap because of band tailing near the contacts; and others (see, for example, Ref. 34, and references therein). For interface-plasmon-mediated anode hole injection a quantitative study has been performed by Fischetti.[34] These calculations predict current ratios of $\alpha_{\text{plasmon}} \lesssim 5 \times 10^{-3}$ in thick films ($t_{\text{ox}} > 50$ nm) at fields around 10 MV/cm. These calculations also predict that such interface processes require less energetic electrons $E_{\text{th}} \lesssim 6$ eV (with Si and Al as anode materials) than impact ionization ($E_{\text{th}} \gtrsim 9$ eV). Combining these predictions with our calculations, it becomes obvious that anode injection will dominate over

impact ionization in thin films and/or at low fields at least qualitatively as reported in Fig. 13. To illustrate this point further, let us consider the 13-nm data in Fig. 13. At this thickness, our calculation (dashed curve) predicts no impact ionization below 12 MV/cm. If we therefore assume that the measured hole currents are entirely due to anode injection, it can be seen that α_{anode} increases from 2×10^{-3} to 6×10^{-3} in the measured field range. These values are somewhat smaller than the values predicted with the "plasmon model" in the steady-state, thick-films limit.[34] This is expected. The plasmon excitation cross section depends strongly on the electron energy at the anode. Therefore, the dark space will reduce hot-electron-induced gate injection in a similar way as it reduces impact ionization, irrespective of the details of the injection mechanism. It would be of interest to reevaluate various gate-injection mechanisms on the basis of the extended transport model introduced here and to calculate its thickness dependence. Additional information on the relative contributions of impact ionization and anode hole injection can be obtained by simultaneously measuring hole trapping in the oxide, as outlined in Sec. IV D.

C. Impact-ionization coefficient

In Fig. 14(a), the impact-ionization coefficients calculated via Eqs. (4) and (6)–(8) in the thick-film limit ($t_{ox} < 100$ nm) are shown as a function of the electric field (upper, heavy, solid curve). For comparison, the apparent ionization coefficient predicted to be measurement by a carrier separation experiment at $t_{ox} = 50$ nm (lower, solid curve) is also shown. As can be seen, α has not yet fully reached its steady-state value at 50 nm and oxide thicknesses of more than 50 nm have to be used in experiments to avoid a strong underestimation of α because of the dark space. These calculated values compare favorably with ionization coefficients derived via Eqs. (10) and (4) from the above carrier separation experiments for oxide thicknesses of 52 (open dots), 67 (diamonds), and 97 nm (triangles). For comparison, we also show the impact-ionization coefficients derived by Solomon and Klein[71] using a current transient technique in MOS capacitors with oxide thicknesses from 30 to 300 nm (heavy dashed line), by Knoll, Bräunig, and Fahrner[72] using a combination of charge injection and irradiation on 150-nm oxides, by Nissan-Cohen, Shappir, and Frohman-Bentchkowsky[73] using charge injection on oxide thicknesses from 17 to 85 nm, and by Chen, Holland, and Hu also using charge injection but in oxides of 13.3 and 20 nm. Among all of these earlier results, the data of Solomon and Klein agree best with our calculations. The completely different field dependences and the much lower values for α_{exp} derived by Chen, Holland, and Hu originate in the use of very thin oxides. This is illustrated

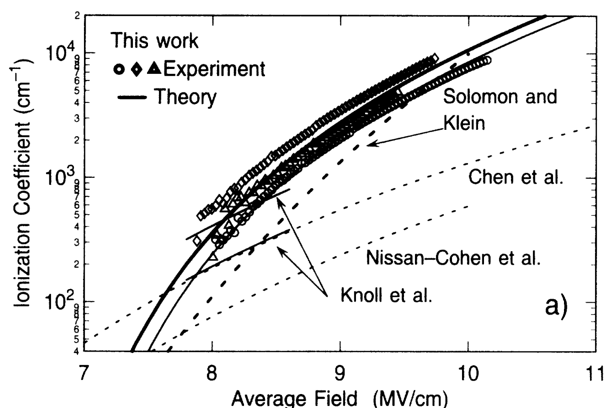

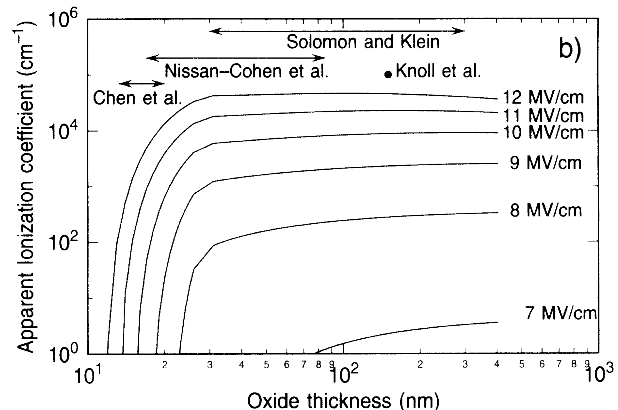

FIG. 14. The top panel (a) shows a comparison of calculated and measured impact-ionization coefficients as a function of electric field. The heavy solid curve (theory) shows the calculated ionization coefficient in the thick-film limit, while the parallel thinner curve shows the apparent ionization coefficient as predicted for a measurement on a 50-nm-thick film. These values are smaller because the dark space cannot be neglected at this thickness. The symbols show experimental values obtained by the carrier separation technique with oxide thicknesses of 52 nm (open dots), 67 nm (diamonds), and 97 nm (triangles). As a correction for generation-recombination currents, a constant value of 10^{-3} was subtracted from the measured current ratios of Fig. 13 before calculating the ionization coefficients. For comparison, we also show the impact-ionization coefficients previously derived by Solomon and Klein (Ref. 71) using a current transient technique in MOS capacitors with oxide thicknesses from 30 to 300 nm (heavy dashed line), Knoll, Bräunig, and Fahrner (Ref. 72) using a combination of charge injection and irradiation on 150-nm oxides, Nissan-Cohen, Shappir, and Frohman-Bentchkowsky (Ref. 73) using charge injection in oxides with thicknesses from 17 to 85 nm, and Chen, Holland, and Hu (Ref. 68) also using charge injection but in oxides with thicknesses of 13.3 and 20 nm. The reasons for the differences between the experimental results are explained in the text. The bottom panel (b) shows the calculated apparent ionization coefficient as it would result from measurements at different oxide thicknesses. Curves for electric fields from 7 to 12 MV/cm are shown. The figure serves to illustrate how the dark space reduces impact ionization in thin films because electron heating has not yet reached steady state. The thickness ranges used in the various experiments of panel (a) are indicated. Only the data of Solomon and Klein (Ref. 71), Knoll, Bräunig, and Fahrner (Ref. 72), and our own measurements (Ref. 32) are not too strongly affected by transient electron heating. (The slight decrease of the ionization coefficient at 12-MV/cm above 200 nm shows the limitations of the analytical equations for the electron multiplication factors as derived from the Monte Carlo results in Fig. 7.)

in detail in Fig. 14(b), where the calculated, *apparent* ionization coefficients by using Eqs. (6)–(8) in combination with Eq. (4)—ignoring the fact that impact ionization is a function of thickness as in Eq. (5) because of transient electron heating—are shown as a function of oxide thickness for various electric fields. The thickness range used for the various experimental studies shown in panel (a) are marked in panel (b). As can be seen from panel (b), for $t_{ox} < 25$ nm, we predict a strong suppression of impact ionization because the electron-energy density has not yet reached steady state and the *apparent* ionization coefficient is a strong function of the oxide thickness. For example, at 10 MV/cm, we predict no impact ionization for thicknesses below 15 nm. Most likely, the occurrence of hole trapping, as observed by Chen, Holland, and Hu and Nissan-Cohen, Shappir, and Frohman-Bentchkowsky in these thin films has to be associated with anode hole injection as discussed in the context of Fig. 13. Chen, Holland, and Hu also speculated that band tailing might play a role. Nissan-Cohen, Shappir, and Frohman-Bentchkowsky were the first to include a dark space for impact ionization in their data analyses. However, their model considerably underestimates the width of the dark space, leading to large errors in the derived ionization coefficients. Below, we show that positive charge buildup *in thick oxides* is indeed caused by impact ionization and the phenomenon can be used to determine impact-ionization coefficients as proposed by Solomon and Klein.[71]

D. Hole trapping

A small fraction of the holes produced by impact ionization (and/or anode injection) are known to get trapped in preexisting hole traps (possibly related to oxygen vacancies) near the Si/SiO_2 interface. This positive charge buildup can be directly measured using capacitance-voltage techniques.[32] The density of the trapped positive charge, p, is entirely controlled by the charge flow through the gate oxide and can be described by the following rate equation,

$$e\frac{dp}{dt} = J_n(m-1)\sigma_p(N_p - p) - J_n\sigma_n p \ . \tag{11}$$

t is the time, e is the magnitude of the electron charge, and N_p is the density of neutral, preexisting hole traps ($\simeq 5\times 10^{12}$ in the samples studied here). J_n is the Fowler-Nordheim current.[74] σ_p is the hole capture cross section with a measured value of $1-2\times 10^{-14}$ cm^2. σ_n is the electron capture cross section of a trapped hole and has measured values of $\sigma_n = 1.28\times 10^{-13} F_{ox}^{-3}$ cm^2 at fields larger than 3 MV/cm.[75] The field, F_{ox}, is in MV/cm. Assuming no trapped holes at $t=0$, the solution to Eq. (11) is

$$p = N_p \frac{(m-1)\sigma_p}{(m-1)\sigma_p + \sigma_n} \times \left[1 - \exp\left[-\frac{J_n}{e}[(m-1)\sigma_p + \sigma_n]t\right]\right] \ . \tag{12}$$

Figure 15 shows a comparison of the calculated and measured positive charge buildup versus the total electron charge, $Q = J_n t/e$, flowing through 24.5- (open dots) and 67-nm (full dots) gate oxides at an average field of 9 MV/cm. Electrons are injected from the silicon substrate. The curves show calculations using Eqs. (6)–(8) and (12). The strong thickness dependence of the positive charge buildup directly reflects the thickness dependence of the electron multiplication factor, m. The saturation values of the calculated curves at large injected charge values correspond to the steady-state situation, in which the same number of holes are trapped per unit time as there are holes annihilated by electron capture. As can be seen from Fig. 15, Eq. (12) seems to breakdown at large electron fluencies. The 24.5-nm data, for example, shows an apparent decrease of the positive charge above fluencies of about 10^{-2} C/cm and a charge sign reversal at 10^{-1} C/cm. These effects are due to charge compensation caused by trap creation (generation of new electron traps) and electron trapping.[32] The negative charge trapped near the SiO_2/Si interface masks the trapped-hole density in the electrical measurements. It is possible to show that the trapped-hole density remains constant—as expected from Eq. (12)—even at high fluencies where the measurements in Fig. 15 show net negative charge.[32]

In Fig. 16, we compare calculated, normalized steady-state, hole densities, p_{sat}/N_p (curves), with the measured saturation values (symbols) over a wide electric field and oxide thickness range. The measured values were obtained from data similar to that shown in Fig. 15 (Ref. 32). The calculated values were obtained via the high fluency limit of Eq. (12):

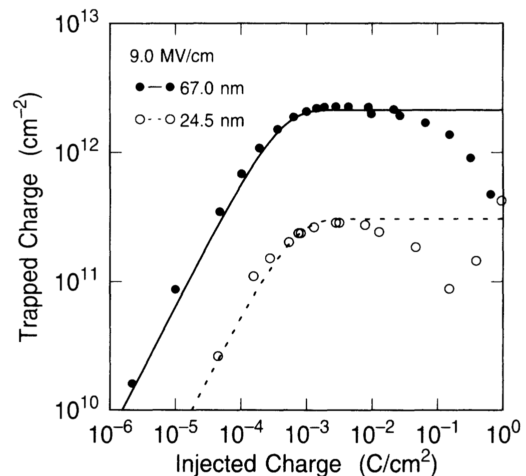

FIG. 15. Comparison of the calculated [Eq. (12), curves] and the measured (symbols) absolute values of the net trapped-charge density near the Si/SiO_2 interface as a function of the injected electron charge into oxides with thicknesses of 24.5 and 67 nm at a field of 9 MV/cm. Equation (12), which accounts for hole generation and hole trapping due to impact ionization, predicts the correct fluency, field, and oxide thickness dependence of the positive charge buildup. The deviations at large fluencies arise because of electron-trapping leading to charge compensation and eventually to a net negative charge (see text).

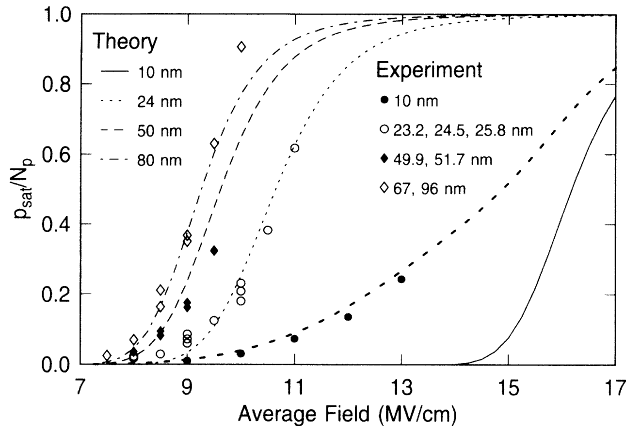

FIG. 16. Comparison of calculated [Eq. (13), curves] and measured (symbols) normalized, steady-state trapped-hole densities, p_{sat} as a function of electric field for oxide thicknesses from 10 to 96 nm. The values shown are normalized to the measured aerial density of hole traps, N_p. The experimental values represent the saturation values as measured from data like that shown in Fig. 15. No hole trapping due to impact ionization is predicted in the 10-nm oxide below 14 MV/cm (solid curve). The observed hole trapping in the 10-nm film may be due to anode-hole injection. This is illustrated by the heavy-dotted line, which shows the steady-state trapped-hole density predicted by Eq. (13), if the as-measured current ratios, α, of the 8-nm oxide from Fig. 13 are used instead of the calculated hole-generation factors, $m-1$ (for details, see text).

$$\frac{p_{sat}}{N_p}=\left[1+\frac{\sigma_n}{(m-1)\sigma_p}\right]^{-1}. \tag{13}$$

Calculated curves for thicknesses of 80, 50, 24, and 10 nm are shown in Fig. 16. The measured field and thickness dependences (arising entirely from the field and thickness dependence of the electron multiplication factor, m) are well accounted for by the calculations for $t_{ox}\geq 20$ nm. In contrast to the experimental findings, the calculations predict no measurable hole trapping below 14 MV/cm in the 10-nm sample shown in Fig. 16. Experimentally, a positive charge buildup with a similarly weak field dependence has also been found under conditions where the total voltage drop across the oxide does not exceed 9 V, making impact ionization impossible.[32,34,67,73] As discussed in the context of Fig. 13, this measured "extra" charge is most likely related to hole injection near the anode. The following comparison of the results in Figs. 13 and 16 strongly supports this supposition. The steady-state hole densities measured in the 10-nm film (full dots in Fig. 16) can be calculated via Eq. (13) simply by using the measured α_{exp} values from Fig. 13 instead of the calculated hole generation factors, $m-1$, for impact ionization. Using the 8-nm data from Fig. 13 in Eq. (13) yields the charge buildup shown by the heavy-dashed line in Fig. 16, consistent with the measured hole densities in the 10-nm oxide. As discussed in Ref. 32, *irreversible* GR currents are of the same order of magnitude as the anode hole currents. This may explain why the 8-nm data from Fig. 13 yields good agreement; GR currents do not flow through the oxide and, therefore, cannot give rise to hole trapping. Also, the hole injection efficiency appears to depend on the gate material and its morphology and the process induced hole-trap density decreases with thickness and cannot easily be measured in thin oxides. All these factors considerably complicate the interpretation of hole trapping in thin films, where impact ionization in the oxide is not the dominant source for holes.

To further illustrate how measurements of hole trapping in the oxide can help to clarify the uncertainties concerning the origin of substrate hole currents, we consider thicker films, where impact ionization is expected to occur simultaneously with anode hole injection because the latter process has a smaller energy threshold. To separate these two different contributions, we make use of the asymmetry in the distribution of hole traps across the oxide films. Hole traps are known to be located near the silicon substrate: The charge centroid for trapped holes is located about $t_c=5$ nm away from the oxide/substrate interface.[32] For positive gate polarity (electron injection from the substrate), all the holes produced by impact ionization are swept past the hole-trap distribution before they are collected in the substrate (see schematic in Fig. 12). For negative gate polarity (injection from the gate), however, a large fraction of the holes produced by ionization will be produced "in front" of the hole-trap distribution and they are never swept past it on their path to the gate. In contrast, holes injected from the contacts are swept across the whole oxide film for both polarities. Therefore, no asymmetry is expected for the trapping of holes produced by anode hole injection. (An asymmetry may arise from variations in the hole injection efficiencies for various contacts.[32]) In Fig. 17, we compare calculat-

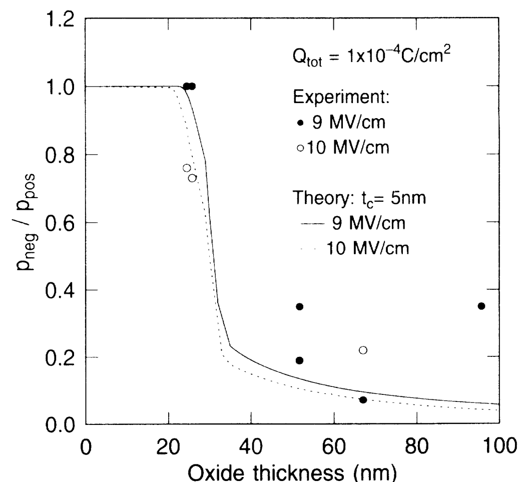

FIG. 17. Polarity dependence of the trapped-hole density near the Si/SiO_2 interface as a function of oxide thickness at fields of 9 and 10 MV/cm. p_{pos} is the trapped-hole density measured after injection from the substrate (positive gate). p_{neg} is the trapped-hole density measured after injection from the gate (negative gate). The injected charge was 1×10^{-4} C/cm^2 in all cases. For the calculations, it was assumed that all hole traps are located at the centroid position of the measured trapped hole distribution, t_c, 5 nm away from the Si/SiO_2 interface.

ed and measured ratios of the trapped-hole densities for the two polarities as a function of oxide thickness at two different field values. The measurements were done by injecting 1×10^{-4} C cm^{-2} for each polarity and field.[32] p_{pos} and p_{neg} corresponds to the charge measured after injection from the substrate and from the gate, respectively. The calculations were done by assuming that all hole traps are located at the centroid position t_c. The trapped-hole ratio can then be calculated as

$$\frac{p_{neg}}{p_{pos}}=\frac{p(m_{neg})}{p(m_{pos})}, \tag{14}$$

where the function $p(m)$ is the trapped hole density as given by Eq. (13). The effective "hole generation factors," $m_{neg}-1=m(t_{ox})-m(t_{ox}-t_c)$ and $m_{pos}-1=m(t_{ox})-m(t_c)$ for the negative and the positive polarity case, respectively, are calculated using Eqs. (6)–(8). As can be seen from Fig. 17, the calculated trapped-hole ratios (curves) rapidly decrease for oxide thickness larger than 25 nm, as experimentally observed (symbols). This transition around 25 nm cannot easily be explained with a gate-injection mechanism alone. In thick films, 50–100 nm, the measured charge ratios appear to be larger than the calculated values on average. This may be related to a symmetric component arising from anode hole injection. A rough estimate of such a component from the deviations between the experimental and the theoretical data yields a value of $\alpha_{anode}\simeq2\times10^{-3}$ to 4×10^{-3} at fields between 9 and 10 MV/cm. These numbers are fairly consistent with the "plasmon model" in the thick-film limit, which predicts values of $\alpha_{plasmon}\simeq1\times10^{-3}$ to 5×10^{-3} in the same field range.[34]

E. Interface-state generation

Trapped-hole–free-electron recombination near the silicon substrate has been shown to lead to interface-state generation at the Si/SiO_2 interface.[33] Since the electron-hole recombination rate for constant current stress is equal to $J_n\sigma_n p/e$ [second term in Eq. (11)], the interface-state generation rate would be expected to be proportional to the positive charge, p, as given by Eq. (12). Qualitatively, such a similarity between hole trapping and interface-state generation has indeed been reported in Ref. 32. An accurate calculation of the interface-state buildup is, however, difficult because the conversion efficiency (the number of interface states generated per recombination event) can vary by as much as three orders of magnitude, depending in a still poorly understood manner on sample processing. Also, the presence of the trapped hole itself appears to induce an interface-statelike response in capacitance-voltage measurements.[76] Finally, interface-state generation via hot-electron-induced hydrogen release is another efficient degradation process (see Sec. V).

F. Temperature dependence

Substrate hole currents and hole trapping have been reported to be essentially temperature independent.[32] Based on our interpretation, this implies that impact ionization in SiO_2 does not significantly depend on temperature. These observations differ from experimental and theoretical findings in semiconductors.[53] An answer to this unexpected behavior in SiO_2 was recently obtained by Eklund, McFeely, and Cartier,[77] using soft-x-ray induced low-energy electron transmission experiments. These studies demonstrated that electron scattering with acoustic phonons is independent of temperature for electron energies above 6 eV. As demonstrated in Sec. III C, the absolute magnitude of the electron multiplication factors are mostly controlled by acoustic scattering at exactly these high energies, explaining the temperature independence of ionization related transport phenomena. Consequently, Eqs. (6)–(8) also provide a good estimate for multiplication factors at low and high temperatures. The unusual behavior of the electron-phonon-scattering rates reported by Eklund, McFeely, and Cartier is believed to be caused by a quantum-mechanical effect,[77] prohibiting the calculation of the temperature dependence of the acoustic electron-phonon-scattering rates at high energies via the Bose factor in Eq. (1a). At energies below about 3 eV, however, the electron-phonon-scattering rates are expected to be temperature dependent as dictated by Eq. (1a). In this energy range, the scattering rates are more than an order of magnitude smaller than at higher energies, such that first-order perturbation theory should still apply.

V. DEGRADATION AND BREAKDOWN OF THIN SiO_2 FILMS ON SILICON

As outlined in the introduction, dielectric breakdown in thin SiO_2 films has almost exclusively been considered to be the result of impact ionization.[1–6,8,9,68,78,79] The success of our transport model justifies a reevaluation of this viewpoint since oxide reliability poses considerable constraints on the operation of many Si/SiO_2-based electronic devices. This is especially true for nonvolatile memory devices, in which high-field electron transport through SiO_2 gates is not merely an undesired side effect but is basic to their operation. The operational conditions, under which impact ionization in an oxide film will have *no* effect on the performance of a floating gate memory cell, for example, are given by the threshold field for ionization as plotted in Fig. 18 (curves labeled "ionization"). The symbols (diamonds) show the threshold fields obtained by Monte Carlo calculations, while the heavy curve (labeled "MC") represents the parametrized result according to Eq. (7). The thin-continuous curve (labeled "ballistic") is the field at which electrons with energies in excess of 9 eV would be observed in the absence of acoustic-phonon scattering. As can be seen, the threshold field for ionization rapidly increases with decreasing oxide thickness. For example, for $t_{ox}<10$ nm, impact ionization does not happen at fields below about 13 MV/cm. Since oxides of 10 nm or thinner will be used in future device generations, impact ionization will be of no concern for device degradation.

The threshold field for impact ionization, F_{th}^{ii}, represents a lower bound to the breakdown field, F_{bd}, predicted by all models based on impact ionization. In

Fig. 18, typical values for F_{bd} from the literature are shown for comparison. The open circles show values measured by DiStefano and Shatzkes in the seventies.[80] The full dots show more recent results (field for 50% failure after 1-sec-stress time) by Ozawa and Yamabe.[81] As can be seen, thick oxides break down well above F_{th}^{ii} suggesting that ionization-induced breakdown might in fact occur. A number of such models have been outlined in the 1970s.[1–6,8,9] Breakdown was proposed to occur because of avalanche multiplication directly. Also, positive feedback models have been explored where enhanced current injection is caused by transient hole-space-charge formation or alternatively by hole trapping. However, using our transport model, we find that none of these mechanisms does apply at the breakdown fields shown in Fig. 18. (Only at much higher fields, some of the above scenarios are expected to apply.) As discussed above, impact ionization is strongly reduced as compared to earlier estimates, yielding $\alpha t_{ox} < 0.1$ at the measured breakdown fields, which is too small a number to cause an avalanche. This number is also too low to cause significant transient positive space charge because the generated holes get swept out of the oxide with a mobility of 2×10^{-5} $cm^2 V^{-1} sec^{-1}$.[70] Even if hole trapping is included, current runaway does not occur at such low fields. Typical hole-trap densities near the silicon/silicon dioxide interface are 5×10^{12} cm^{-2}. Most of these traps are filled

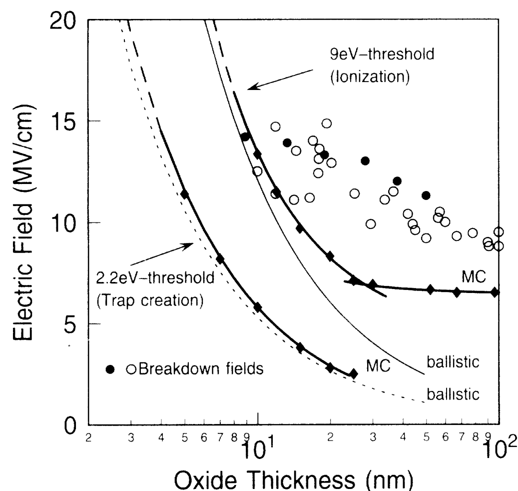

FIG. 18. Calculated threshold fields for impact ionization in SiO_2 [9 eV threshold (ionization)], and for defect generation by the "*trap creation*" process [2.2-eV threshold (trap creation)]. "*Trap creation*" refers to defect generation caused by hot-electron induced hydrogen release (Ref. 86). The symbols (diamonds) represent values obtained directly from Monte Carlo simulations, while the heavy solid curve (MC) represents a numerical interpolation of the Monte Carlo results [Eq. (7) for impact ionization]. For both processes, the hypothetical threshold fields for ballistic transport in the oxide—no phonon scattering—are shown for comparison (ballistic). The dramatic influence of acoustic scattering on the ionization threshold in thick films can be clearly seen by comparing the calculations (MC and ballistic). Measured breakdown fields (open circles and dots) from Refs. 80 and 81 are shown for comparison.

well before breakdown occurs, leading to measured transient current increases which are too small to destroy the oxide.[32] Also, the positive charge becomes rapidly compensated by electrons trapping and net negative trapping is observed near breakdown.[82] Finally, from Fig. 18, it can be seen that the measured breakdown fields do not follow the calculated thickness dependence of F_{th}^{ii}—the thinnest films fail at fields at which ionization is barely possible. It has been proposed that anode hole injection might provide enough holes for breakdown to occur in these thin films.[79] Based on the discussions in this paper, it is unlikely that anode hole injection can provide enough positive charge for current runaway and breakdown. In summary, all of these considerations strongly suggest that breakdown models involving impact ionization and hole trapping do not apply at the low breakdown fields typically measured in SiO_2 films during current stress.

Based on the original proposal by Harari,[82] we recently developed quite a different degradation and breakdown concept which does not suffer from the limitations of breakdown models which are solely based on hole trapping in the oxide. We proposed[83] that *breakdown might be the result of cumulative hot-electron-induced degradation of the oxide film near its interfaces. The degradation is proposed to be caused by "trap creation"*[84-89] *and electron-hole recombination*[33] *together.* The basic idea is simply that both of these processes continuously degrade the oxide quality in the interfacial, stressed regions—breaking oxide bonds by hot-electron-initiated chemical reactions as specified below—until the thin-film structure becomes inherently unstable.

The term "*trap creation*" refers to the following four-step degradation sequence.[84–86,88] Injected electrons heat up on their pass through the oxide (step 1) and liberate processing-induced hydrogen by hot-electron impact (step 2) mostly near the anode because process induced hydrogen is concentrated at the interfaces. A minimum electron energy of less than 2 eV with respect to the bottom of the oxide conduction band is required for hydrogen release.[84,86] The liberated hydrogen, assumed to be H^0 (neutral hydrogen), then diffuses through the oxide (step 3). Hydrogen redistribution during high-field current stress has been observed directly by hydrogen profiling techniques.[90,91] Finally, H^0 can react chemically with precursor sites to generate various kinds of defects (step 4). These defects can be observed by electrical measurements as anomalous positive charge, oxide electron traps, and interface states.[85,86] In recent electron-spin resonance studies,[92,93] the P_bH defect, which is the hydrogen-passivated P_b center, has been identified as one specific precursor site that reacts with atomic hydrogen; the interface state, known as the silicon dangling bond or P_b center, is produced by the reaction, $P_bH+H^0 \rightarrow P_b+H_2$. These studies also showed that other kinds of defects, distributed away from the interfaces are produced by this four-step process. It has recently been demonstrated that the degradation during high-field current stress shows striking similarities with the atomic hydrogen-induced degradation during remote hydrogen-plasma exposure.[94] "*Trap creation*" occurs efficiently also

in very thin oxides and at fields far below the impact ionization threshold.[85–89] These points are illustrated in Fig. 18, where the calculated threshold field for "*trap creation*" (here a 2.2-eV threshold as an upper limit for the onset of the phenomena was used) is compared to the ionization threshold. The symbols (diamonds) show results of our Monte Carlo calculation. The heavy curve (labeled "MC") is a numerical interpolation between these values. The dashed curve (labeled "ballistic") shows the field, at which electrons with energies in excess of 2.2 eV would be observed in the absence of phonon scattering. It can be seen that breakdown occurs far above the "*trap creation*" threshold at all oxide thicknesses.

With decreasing field and with decreasing oxide thickness, "*trap creation*" will inevitably become the dominant degradation mode. These transitions from the impact-ionization regime into the "*trap creation*" regime are discussed below in detail, using the interface-state generation and the charge to breakdown (CTB) measured in time-dependent breakdown as examples. It is our intention to illustrate that *the proposed degradation and breakdown concept has considerable predictive power if it is formulated within the transport model introduced in this paper.* We have no intention to prove its validity under all possible conditions, such as processing variations, polarity dependences, or temperature dependences. However, we express the degradation process in terms of the hot-electron dynamics and in terms of physical quantities such as the hydrogen concentration and distribution, the hydrogen diffusion, the density of process induced hole traps, and so on, which can be measured independently. It is therefore possible to qualitatively evaluate the consistence of our proposal with results obtained by varying the conditions mentioned. On that qualitative level, matters appear to be consistent. The hydrogen chemistry is treated phenomenologically. It can, however, be incorporated on a microscopic level as more information becomes available.

We start out by predicting the field and thickness dependence of the interface-state generation rate, which is defined as the number of interface-states generated per unit of injected electron charge.[83] As can be seen from Fig. 19 [panel (a)], these rates vary over several orders of magnitude both as a function of thickness at constant field and likewise as function of field at constant oxide thickness. These dramatic variations can be understood on the basis of our transport model using the proposed degradation concept. The interface-state generation rate due to "*trap creation*" during current stress under positive gate bias (electron injection from the Si substrate) is expressed on the basis of the four-step model as follows:[84]

$$\frac{dn_{\rm it}^{\rm tc}}{dt}=\gamma_d\sigma_r[S_p]\frac{J_n}{e}[N_H]\int_0^\infty \sigma_{\rm bb}(E)n(E)dE \ , \quad (15a)$$

where $[N_H]$ is the aerial hydrogen concentration at the oxide-anode interface. $\sigma_{\rm bb}(E)$ is the bond-breaking (or hydrogen release) cross section. The quantity $[S_p]$ is the aerial density of precursor sites at the Si/SiO_2 interface which can be transformed into electrically active defects by reacting with liberated atomic hydrogen. The con-

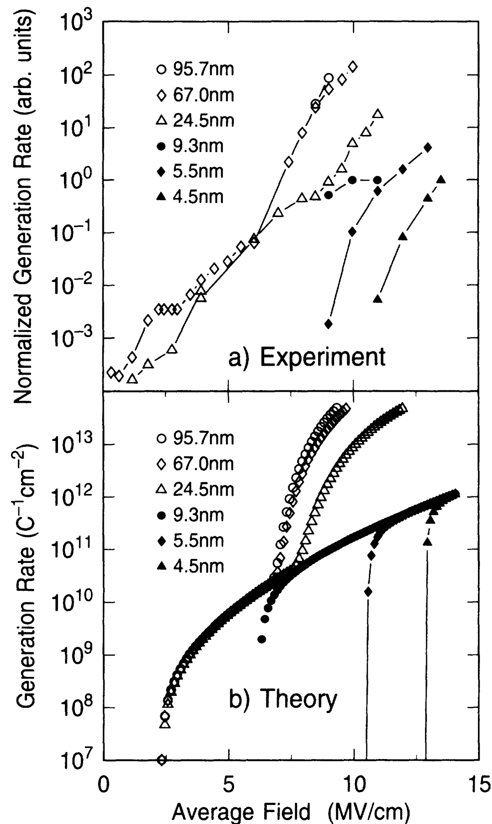

FIG. 19. Comparison of measured [panel (a)] and calculated [panel (b)] interface-state generation rates as a function of electric field for oxide thicknesses from 4.5 to 96 nm. The measured values are from Ref. 82. The calculations are based on Eqs. (15) and (16).

stant γ_d is the probability that a liberated hydrogen atom will diffuse from the gate to the $SiSiO_2$ interface and σ_r is a reaction cross section quantifying the reaction of atomic hydrogen with the precursor site S_p. The energy density near the anode, $n(E)$, is calculated with the Monte Carlo transport program. The energy dependence of the hydrogen-release cross section can be obtained in the following manner.[84] During current stress, simultaneously with the interface-state buildup at the cathode, a buildup of anomalous-positive charge (slow donor-type states) occurs near the anode. We believe that these defects at the anode are the remainder of those impurity sites from which a hydrogen atom has been striped by a hot electron. If this applies, the energy dependence of the hydrogen-release cross section can be determined from the field dependence of the slow-state generation. Using this approach, we find[84]

$$\sigma_{\rm bb}(E)=\sigma_0\left[\frac{E}{E_{\rm th}^{\rm tc}}-1\right]^n , \quad (15b)$$

where $n \simeq 2$ and $E_{\rm th}^{\rm tc} \simeq 1.6$ eV.

The calculation of the interface-state generation by electron-hole recombination is again based on the transport model. We assume that impact ionization is the only source for holes in the oxide. (As discussed previ-

ously, this is an oversimplification because hole currents and hole trapping are also caused by hole injection near the anode. Conceptually, the inclusion of anode hole injection is straightforward. The magnitude of these hole currents, however, is still rather poorly known.) We thus use the equation

$$\frac{dn_{\rm it}^{e\text{-}h}}{dt} = \gamma_{e\text{-}h} \frac{J_n}{e} \sigma_n p(F, t_{\rm ox}) , \quad (16)$$

where $\gamma_{e\text{-}h}$ is the probability that an interface state will be created per electron-hole recombination event[33] and $p(F,t)$ is the trapped-hole density as given by Eq. (11).

To predict the field and thickness dependence from Eqs. (15) and (16), the absolute values for the various factors, $[N_H], \gamma_d, \sigma_r, \sigma_o, [S_p], \gamma_{e\text{-}h}$, are not independently required. We assume all these parameters to be constants, independent of oxide field and thickness and we use typical values of $\gamma_{e\text{-}h}=0.3$, $N_p=5\times10^{12}$ cm^{-2} and we finally adjust the product $\gamma_d \sigma_r [S_p] \sigma_0 [N_H]$, such that 10^{11} interface states are produced per unit of injected charge by "*trap creation*" at 10 MV/cm in a 10-nm-thick film. These values are consistent with parameters measured in the samples used for the experiments in Fig. 19.[86] Using these normalizations, we calculate the pattern shown in panel (b) of Fig. 19. Clearly, panel (b) shows essentially the same pattern as the measured generation rates shown in panel (a).

The strong field and thickness dependences calculated in Fig. 19 arise solely from changes in the electron-energy density, $n(E)$, with field and thickness, all other parameters were assumed to be constant. Let us discuss the 95.7-nm film first. At 2.5 MV/cm, LO-phonon runaway and electron heating to energies larger than the threshold for "*trap creation*" of 1.6 eV (see Fig. 3) causes a rapid onset of interface-state generation. (The experimental data shows interface-state generation at even lower fields. We have direct evidence that this difference is caused by the substrate hot-electron injection used in the experiments as compared to FN injection used in the calculation.) With increasing field, the energy distribution becomes restabilized by acoustic-phonon scattering and the generation rate in Fig. 19 increases slowly, qualitatively following the average electron energy (see Fig. 3). At 7 MV/cm, acoustic runaway occurs causing impact ionization and interface-state generation by electron-hole recombination [Eq. (16)] (and also by hole trapping directly) in addition to "*trap creation*". If the contribution due to Eq. (16) is small or absent, the interface-state generation rate will continue to increase slowly in accordance with the average electron energy, following the 9.3-nm data shown in the figure. The 95.7-nm data below 7 MV/cm and the 9.3-nm data above 7.5 MV/cm define a smooth function which represents the "*trap creation*" result for hydrogen release by an electron distribution which has reached (quasi-) steady state at the gate contact. The variations with thickness can now be understood easily via Fig. 18. As can be seen there, in thinner films, the "*trap creation*" threshold shifts to higher fields (6, 10, and 13 MV/cm for 9.3, 5.5, and 4.5 nm, respectively) and simultaneously the impact-ionization threshold shifts to higher fields as well. In the 9.3-nm oxide shown, impact ionization sets in at 15 MV/cm (see Fig. 18), which is outside the range of Fig. 19. It is interesting to note that the predicted saturation with increasing thickness in the ionization regime (the data for the 67- and 95.7-nm oxides are almost identical) is also apparent in the experimental data. This simply reflects the transition to steady-state impact ionization outside the 30-nm range of the dark space.

As a second and final example, we demonstrate that the cumulative degradation caused by "*trap creation*" and electron-hole recombination together allows some intriguing predictions for the field and thickness dependence of the total CTB. Again, the calculation of absolute CTB values would require a detailed understanding of the microscopic degradation processes. For example, it is not clear which defects are most relevant for the degradation that leads to breakdown. Harari[82] concluded that distributed electron traps may be more important than interface states. Experimentally, the generation of distributed electron traps and the generation of interface states follow a very similar pattern. Therefore, we simply use the interface-state density as an indicator or measure for the cumulative oxide damage during current stress. We postulate that the oxide becomes prone to failure when the interface-state density reaches a critical value of 5×10^{13} cm^{-2}. (We find by trial and error that this hypothetical breakdown criterion yields absolute values for the CTB which are comparable with measured values.) Using this criterion, we can now calculate the (hypothetical) charge to breakdown as a function of oxide field and oxide thicknesses simply by integrating Eqs. (15) and (16) together until the critical number of interface states is produced. The results of these calculations are summarized in Fig. 20. The calculated pattern shows all the features observed in the field and thickness dependence of recent CTB measurements,[79,81] strongly supporting the idea that the CTB is determined by the cumulative degradation caused by two distinctly different hot-electron-induced defect creation processes together, namely, electron-hole recombination caused by impact ionization *and* hydrogen release and reaction in the "*trap creation*" process, *and* interface-state generation can be used as an indicator for breakdown. Again, the field and thickness dependence of the CTB is solely a function of the electron dynamics as it evolves from our transport model. All curves converge to or depart from the steady-state trap creation result which decays roughly exponentially with a slope of 0.2 decades/MV. The discussion to Fig. 19 directly applies to Fig. 20 and we leave it to the reader to connect the pattern in Fig. 20 to the details of the hot-electron dynamics. We have used this degradation concept for process optimization.[94] For example, in reoxidized-nitrided oxides we directly showed that nitrogen acts as a scavenger of atomic hydrogen and thus dramatically reduces the probability γ_d for hydrogen diffusion to the Si/SiO_2 interface, decreasing the interface-state generation rate and possibly increasing the CTB values. Also, the effects of the actual hydrogen distribution as measured by nuclear reaction analyses, for example, can be directly studied.[84]

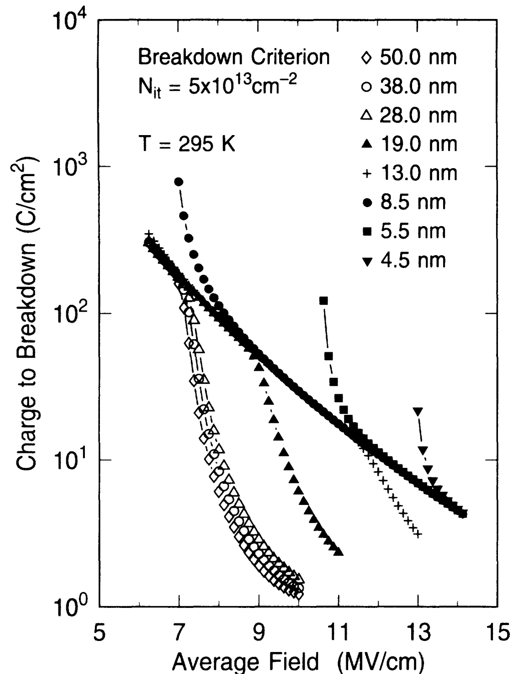

FIG. 20. Calculated total charge required to flow through a SiO_2 gate oxide in order to generate 5×10^{13} cm^{-2} interface states by hot-electron degradation according to Eqs. (15) and (16). Calculations for oxide thicknesses from 4.5 to 50 nm and oxide fields from 6 to 14 MV/cm are shown. The figure serves to illustrate how the electron dynamics affects the charge to breakdown if it were determined by cumulative interface degradation caused by "*trap creation*" (hot-electron-induced hydrogen release) and impact ionization together (for details, see text).

VI. CONCLUSIONS

A transport model which is based on electron-phonon-scattering rates derived from zero-field photon-induced electron transmission experiments[27–29,44] has been developed and the hot-electron dynamics has been investigated using a Monte Carlo integration of the transport equation. We demonstrated that the observed decrease in the acoustic scattering rate at high energies[29] leads to an electron runaway phenomenon which we call *acoustic-phonon runaway*. Acoustic runaway was shown to be the key process for a quantitative understanding of impact ionization in SiO_2. We have tested our model by comparing its predictions with results of several high-field transport experiments in SiO_2/Si device structures. We demonstrated that acoustic-phonon runaway accounts for the high-energy tails in the electron-energy distribution as measured by vacuum emission. The calculated electron multiplication factors were shown to account for the oxide field and thickness dependence of hole currents in *n*-channel FET's using the carrier separation technique and for the positive charge buildup (hole trapping) in SiO_2 films during high-field current stress. A detailed comparison of our calculations with existing experimental data strongly suggests that hole currents and hole trapping are also caused by hot-electron-induced hole injection at or near the anode.

The transport model was also used to investigate the importance of impact ionization and hole trapping for dielectric breakdown. We present strong evidence that these processes are of minor importance in thin films because impact ionization is found to be strongly suppressed for oxide thicknesses $t_{ox} < 20$ nm. Our transport model is shown to be compatible with the alternative proposition, by DiMaria, Arnold, and Cartier,[83] that breakdown in such thin films might be the result of the cumulative degradation of the thin film structures near its interfaces caused primarily by hot-electron-induced hydrogen chemistry. The complicated thickness and field dependences of the interface-state generation rate and of the charge to breakdown can be readily calculated on the basis of our transport model, strongly supporting the supposition that the hot-electron-induced hydrogen chemistry might be the limiting factor for the durability of thin oxide films.

ACKNOWLEDGMENTS

The authors would like to thank M. V. Fischetti for providing the Monte Carlo code used in his original calculations and for challenging discussions concerning the relation between impact ionization and anode-hole injection. The authors would like to thank F. R. McFeely, P. J. Price, J. Stathis, D. A. Buchanan, and R. E. Stahlbush for numerous revealing discussions. The assistance of S. E. Laux with computing has been invaluable.

*Present address: Department of Electrical Engineering and Computer Science (M/C 154), 1120 Science and Engineering Offices, University of Illinois at Chicago, 851 S. Morgan St., Chicago, Il 60607.

[1] J. J. O'Dwyer, J. Appl. Phys. **40**, 3887 (1969).
[2] K. K. Thornber and R. P. Feynman, Phys. Rev. B **15**, 4099 (1970).
[3] A. Halim, M. Shousha, D. L. Pulfrey, and L. Young, J. Appl. Phys. **43**, 15 (1972).
[4] W. T. Lynch, J. Appl. Phys. **43**, 3274 (1972).
[5] T. H. DiStefano and M. Shatzkes, Appl. Phys. Lett. **25**, 685 (1974).
[6] N. Klein and P. Solomon, J. Appl. Phys. **47**, 4364 (1976).
[7] N. Klein, Thin Solid Films **50**, 223 (1978).
[8] D. K. Ferry, J. Appl. Phys. **50**, 1422 (1979).
[9] N. Klein, J. Appl. Phys. **53**, 5828 (1976).
[10] P. M. Solomon, in *The Physics of SiO_2 and its Interfaces,* edited by S. T. Pantelides (Pergamon, New York, 1986), p. 35.
[11] M. Shatzkes and M. Av-Ron, J. Appl. Phys. **47**, 3192 (1976).
[12] H. J. Fitting and J. U. Friemann, Phys. Status Solidi A **69**, 349 (1982).
[13] T. N. Theis, D. J. DiMaria, J. R. Kirtley, and D. W. Dong, Phys. Rev. Lett. **52**, 1445 (1984).
[14] D. J. DiMaria, T. N. Theis, J. R. Kirtley, F. L. Pesavento, D. W. Dong, and S. D. Brorson, J. Appl. Phys. **57**, 1214 (1985).
[15] S. D. Brorson, D. J. DiMaria, M. V. Fischetti, F. L. Pesavento, P. M. Solomon, and D. W. Dong, J. Appl. Phys. **58**, 1302 (1985).

[16]B. K. Ridley, J. Appl. Phys. **46**, 998 (1975).
[17]P. M. Mednis and V. M. Fain, Zh. Eksp. Teor. Fiz. **62**, 812 (1972) [Sov. Phys. JETP **35**, 429 (1972)].
[18]A. Epifanov, Zh. Eksp. Teor. Fiz. **67**, 1805 (1974) [Sov. Phys. JETP **40**, 897 (1975)].
[19]L. H. Holway, Jr. and D. W. Fradin, J. Appl. Phys. **46**, 279 (1975).
[20]M. Sparks, D. L. Mills, R. Warren, T. Holstein, A. A. Maradudin, L. J. Sham, E. Loh, Jr., and D. F. King, Phys. Rev. B **24**, 3519 (1981).
[21]M. V. Fischetti, Phys. Rev. Lett. **53**, 1755 (1984).
[22]M. V. Fischetti, D. J. DiMaria, S. D. Brorson, T. N. Theis, and J. R. Kirtley, Phys. Rev. B **31**, 8124 (1985).
[23]W. Porod and D. K. Ferry, Phys. Rev. Lett. **54**, 1189 (1985).
[24]D. K. Ferry, in *The Physics and Technology of Amorphous Silicon Dioxide,* edited by Roderick A. B. Devine (Plenum, New York, 1988), p. 365.
[25]J. N. Bradford and S. Woolf, Radiat. Eff. Defects Solids **117**, 227 (1991).
[26]J. N. Bradford and S. Woolf, J. Appl. Phys. **70**, 490 (1991).
[27]F. R. McFeely, E. Cartier, L. J. Terminello, A. Santoni, and M. V. Fischetti, Phys. Rev. Lett. **65**, 1937 (1990).
[28]F. R. McFeely, E. Cartier, J. A. Yarmoff, and S. A. Joyce, Phys. Rev. B **42**, 5191 (1990).
[29]E. Cartier and F. R. McFeely, Phys. Rev. B **44**, 10 689 (1991).
[30]D. J. DiMaria, D. Arnold, and E. Cartier, Appl. Phys. Lett. **60**, 2118 (1992).
[31]D. Arnold, E. Cartier, and D. J. DiMaria, Phys. Rev. B **45**, 1477 (1992).
[32]D. J. DiMaria, E. Cartier, and D. Arnold, J. Appl. Phys. **73**, 3367 (1993).
[33]S. K. Lai, J. Appl. Phys. **54**, 2540 (1983).
[34]M. V. Fischetti, Phys. Rev. B **31**, 2099 (1985).
[35]P. J. Price, Semicond. Semimet. **14**, 249 (1979).
[36]C. Jacoboni and L. Reggiani, Rev. Mod. Phys. **55**, 645 (1983).
[37]J. R. Chelikowsky and M. Schlüter, Phys. Rev. B **15**, 4020 (1977).
[38]G. Lewicki and J. Maserjian, J. Appl. Phys. **46**, 3032 (1975).
[39]J. Maserjian, J. Vac. Sci. Technol. **11**, 996 (1974).
[40]J. Maserjian and G. P. Peterson, Appl. Phys. Lett. **25**, 50 (1974).
[41]J. Maserjian and N. Zamani, J. Appl. Phys. **53**, 559 (1982).
[42]J. Maserjian, in *The Physics and Chemistry of SiO_2 and the SiO_2 Interface,* edited by C. R. Helms and B. E. Deal (Plenum, New York, 1988), p. 497.
[43]Z. A. Weinberg, J. Appl. Phys. **53**, 5052 (1982).
[44]E. Cartier and P. Pfluger, Phys. Scr. **T23**, 235 (1988).
[45]F. J. Himpsel and D. Straub, Surf. Sci. **168**, 764 (1986).
[46]J. H. Jensen and J. A. Sauls, Phys. Rev. B **38**, 13 387 (1988).
[47]P. A. Thiry, M. Liehr, J. J. Pireaux, R. Sporken, R. Caudano, J. P. Vigneron, and A. A. Lucas, J. Vac. Sci. Technol. B **3**, 1118 (1985).
[48]D. Arnold and E. Cartier, Phys. Rev. B **46**, 15 102 (1992).
[49]D. J. DiMaria and M. V. Fischetti, J. Appl. Phys. **64**, 4683 (1988).
[50]S. I. Zakharov and Y. D. Fiveisky, Solid State Commun. **66**, 1251 (1988).
[51]G. Blatter and F. Greuter, Phys. Rev. B **34**, 8555 (1986).
[52]M. V. Fischetti and S. E. Laux, Phys. Rev. B **38**, 9721 (1988).
[53]M. V. Fischetti, IEEE Trans. Electron Devices **ED-38**, 634 (1991).
[54]M. V. Fischetti and D. J. DiMaria, Phys. Rev. Lett. **55**, 2475 (1985).
[55]K. Kim and K. Hess, J. Appl. Phys. **60**, 2626 (1986).
[56]G. E. Bulman, V. M. Robbins, and G. E. Stillman, IEEE Trans. Electron Devices **ED-32**, 2454 (1985).
[57]E. Cartier, M. V. Fischetti, E. A. Eklund, and F. R. McFeely, Appl. Phys. Lett. **64**, 3339 (1993).
[58]D. J. DiMaria, M. V. Fischetti, E. Tierney, and S. D. Brorson, Phys. Rev. Lett. **56**, 1284 (1986).
[59]D. J. DiMaria, M. V. Fischetti, M. Arienzo, and E. Tierney, J. Appl. Phys. **60**, 1719 (1986).
[60]D. G. Esaev and S. P. Sinitsa, Pis'ma Zh. Tekh. Fiz. **12**, 1063 (1986) [Sov. Tech. Phys. Lett. **12**, 440 (1986)].
[61]D. G. Esaev and S. P. Sinitsa, Pis'ma Zh. Tekh. Fiz. **14**, 913 (1988) [Sov. Tech. Phys. Lett. **14**, 404 (1988)].
[62]H. J. Fitting and A. von Czarnowski, Phys. Status Solidi A **93**, 385 (1986).
[63]L. D. Yau, F. T. Liou and S. Chen, IEEE Electron Dev. Lett. **EDL-4**, 261 (1983).
[64]B. Eitan and A. Kolodny, Appl. Phys. Lett. **43**, 106 (1983).
[65]Z. A. Weinberg, G. W. Rubloff, and E. Bassous, Phys. Rev. B **19**, 3107 (1979).
[66]Z. A. Weinberg and M. V. Fischetti, J. Appl. Phys. **57**, 443 (1985).
[67]Z. A. Weinberg, M. V. Fischetti, and Y. Nissan-Cohen, J. Appl. Phys. **59**, 824 (1986).
[68]I. C. Chen, S. Holland, and C. Hu, IEEE Electron Dev. Lett. **EDL-7**, 164 (1986).
[69]R. C. Hughes, Phys. Rev. B **15**, 2012 (1977).
[70]R. C. Hughes, Solid-State Electron. **21**, 251 (1978).
[71]P. Solomon and N. Klein, Solid State Commun. **17**, 1397 (1975).
[72]M. Knoll, D. Bräunig, and W. R. Fahrner, J. Appl. Phys. **53**, 6946 (1982).
[73]Y. Nissan-Cohen, J. Shappir, and D. Frohman-Bentchkowsky, J. Appl. Phys. **57**, 1375 (1985).
[74]S. M. Sze, *Physics of Semiconductor Devices,* 2nd ed. (Wiley, New York, 1981).
[75]D. A. Buchanan, M. V. Fischetti, and D. J. DiMaria, Phys. Rev. B **43**, 1471 (1991).
[76]D. J. DiMaria (unpublished).
[77]E. A. Eklund, F. R. McFeely, and E. Cartier, Phys. Rev. Lett. **69**, 1407 (1992).
[78]I. C. Chen, S. E. Holland, and C. Hu, IEEE Trans. Electron Dev. **ED-32**, 413 (1985).
[79]I. C. Chen, S. Holland, K. K. Young, C. Chang, and C. Hu, Appl. Phys. Lett. **49**, 669 (1986).
[80]T. H. DiStefano and M. Shatzkes, J. Vac. Sci. Technol. **13**, 50 (1976).
[81]Y. Ozawa and K. Yamabe, in *Extended Abstracts of the 1991 International Conference on Solid-State Devices and Materials* (Jap. Soc. Appl. Phys., Tokyo, 1991), pp. 240–242.
[82]E. Harari, J. Appl. Phys. **49**, 2478 (1978).
[83]D. J. DiMaria, D. Arnold, and E. Cartier, Appl. Phys. Lett. **61**, 2329 (1992).
[84]E. Cartier and D. J. DiMaria, Microelectronic Engineering **22**, 207 (1993).
[85]D. J. DiMaria, Appl. Phys. Lett. **51**, 665 (1987).
[86]D. J. DiMaria and J. W. Stasiak, J. Appl. Phys. **65**, 2342 (1989).
[87]C. T. Sah, Solid-State Electron. **33**, 147 (1990).
[88]D. J. DiMaria, J. Appl. Phys. **68**, 5234 (1990).
[89]T. Nishida and S. E. Thompson, J. Appl. Phys. **69**, 3986 (1991).
[90]F. Feigl, R. Gale, H. Chew, C. Magee, and D. Young, Nucl. Instrum. Methods Phys. Res. Sect. B **1**, 348 (1984).
[91]A. D. Marwick, D. Buchanan, D. J. DiMaria, P. Saunders,

and L. Dori, in *Proceedings of Symposium on Amorphous Insulating Thin Films,* edited by J. Kanicki, W. L. Warren, R. A. B. Devine, and M. Matsurmura (Materials Research Society, Boston, Mass., in press), Vol. 284.

[92]E. Cartier, J. H. Stathis, and D. A. Buchanan, Appl. Phys. Lett. **63**, 1510 (1993).

[93]J. H. Stathis and D. J. DiMaria, Appl. Phys. Lett. **61**, 2887 (1992).

[94]E. Cartier, D. A. Buchanan, and G. J. Dunn, Appl. Phys. Lett. **64**, 901 (1994).